



Analysis of Erosion Transition in Tungsten-Alloy Rods Into Aluminum Targets

by Steven B. Segletes

ARL-TR-3153

March 2004

NOTICES

Disclaimers

The findings in this report are not to be construed as an official Department of the Army position unless so designated by other authorized documents.

Citation of manufacturer's or trade names does not constitute an official endorsement or approval of the use thereof.

Destroy this report when it is no longer needed. Do not return it to the originator.

Army Research Laboratory

Aberdeen Proving Ground, MD 21005-5066

ARL-TR-3153**March 2004**

Analysis of Erosion Transition in Tungsten-Alloy Rods Into Aluminum Targets

Steven B. Segletes
Weapons and Materials Research Directorate, ARL

Report Documentation Page				Form Approved OMB No. 0704-0188	
Public reporting burden for this collection of information is estimated to average 1 hour per response, including the time for reviewing instructions, searching existing data sources, gathering and maintaining the data needed, and completing and reviewing the collection information. Send comments regarding this burden estimate or any other aspect of this collection of information, including suggestions for reducing the burden, to Department of Defense, Washington Headquarters Services, Directorate for Information Operations and Reports (0704-0188), 1215 Jefferson Davis Highway, Suite 1204, Arlington, VA 22202-4302. Respondents should be aware that notwithstanding any other provision of law, no person shall be subject to any penalty for failing to comply with a collection of information if it does not display a currently valid OMB control number. PLEASE DO NOT RETURN YOUR FORM TO THE ABOVE ADDRESS.					
1. REPORT DATE (DD-MM-YYYY) March 2004		2. REPORT TYPE Final		3. DATES COVERED (From - To) October 2000–September 2003	
4. TITLE AND SUBTITLE Analysis of Erosion Transition in Tungsten-Alloy Rods Into Aluminum Targets				5a. CONTRACT NUMBER	
				5b. GRANT NUMBER	
				5c. PROGRAM ELEMENT NUMBER	
6. AUTHOR(S) Steven B. Segletes				5d. PROJECT NUMBER AH80	
				5e. TASK NUMBER	
				5f. WORK UNIT NUMBER	
7. PERFORMING ORGANIZATION NAME(S) AND ADDRESS(ES) U.S. Army Research Laboratory ATTN: AMSRD-ARL-WM-TD Aberdeen Proving Ground, MD 21005-5066				8. PERFORMING ORGANIZATION REPORT NUMBER ARL-TR-3153	
9. SPONSORING/MONITORING AGENCY NAME(S) AND ADDRESS(ES)				10. SPONSOR/MONITOR'S ACRONYM(S)	
				11. SPONSOR/MONITOR'S REPORT NUMBER(S)	
12. DISTRIBUTION/AVAILABILITY STATEMENT Approved for public release; distribution is unlimited.					
13. SUPPLEMENTARY NOTES					
14. ABSTRACT This work extends and refines the phenomenological understanding of ballistic penetration in the vicinity of the erosion-threshold velocity, for the case of hemispherical-nosed tungsten rods striking ductile targets. Analysis, supported by experimentation, indicates a period of noneroding penetration for these configurations, which results from lateral support exerted by the target crater upon the deforming, yet noneroding, penetrator. Experiments indicate that the magnitude of the lateral support, the direct result of an interference fit between rod and crater, must be on the order of the target's ballistic-penetration resistance, and does not vary with the impact velocity over the range studied. Analysis suggests that the duration of the noneroding portion of the ballistic event is neither governed by a fixed time, nor by a fixed depth of penetration, but rather by a fixed, permissible level of deformation in the penetrator.					
15. SUBJECT TERMS erosion, noneroding, transition, threshold, aluminum, long rod, hemispherical nose, ballistics					
16. SECURITY CLASSIFICATION OF:			17. LIMITATION OF ABSTRACT UL	18. NUMBER OF PAGES 60	19a. NAME OF RESPONSIBLE PERSON Steven B. Segletes
a. REPORT UNCLASSIFIED	b. ABSTRACT UNCLASSIFIED	c. THIS PAGE UNCLASSIFIED			19b. TELEPHONE NUMBER (Include area code) 410-306-1939

Contents

List of Figures	iv
List of Tables	v
1. Introduction	1
2. Observations	3
3. Modeling	6
3.1 Trigger for Erosion	10
3.2 H_{LAT} Magnitude.....	13
3.3 Impact Pressure	13
3.4 Plastic Zone Size in Rod.....	15
3.4.1 Equation of Noneroding Rod Motion.....	15
3.4.2 Extended Bernoulli Equation	16
3.5 Integration of Rod Deformation	19
4. Modeling Results	20
5. Comparison to FZ Model	25
6. Conclusions	33
7. References	35
Distribution List	38

List of Figures

Figure 1. Penetration and residual-velocity data into 344 mm monolithic Al (BHN 97). For comparison, model results for rigid and eroding rods are included.....	2
Figure 2. Schematic showing how lateral confinement may augment the axial stress brought to bear by the rod, in light of plastic yield condition.	7
Figure 3. Data for Finite-Target Series tests, with comparison to rigid-model and eroding-model calculations, for (a) residual rod length and (b) residual velocity.	9
Figure 4. Radiographic image of residual rod from test MV7, depicting intact nose and fractured tail (note: rod is moving left to right on image).	9
Figure 5. Data for Interply Series tests, with comparison to rigid-model and eroding-model calculations, for (a) residual rod length and (b) residual velocity.	10
Figure 6. Back-calculated “effective” velocity-dependent rod strength, to accurately model residual length in Finite-Target Series tests, assuming effective strength was to act over full duration of ballistic event.	11
Figure 7. Photograph depicting residual-rod fragment recovered from test MV1. While rod tip appears undeformed, measurement reveals a 6% increase in rod diameter.	12
Figure 8. Schematic depicting the axial-stress levels at three locations, A, B, and T along the rod centerline, along with two versions of the rod-deceleration equation (one requiring knowledge of s , the other not).....	17
Figure 9. Data for Finite-Target Series tests, with comparison to revised-methodology calculation, for (a) residual rod length and (b) residual velocity.	21
Figure 10. Data for Semi-Infinite Series I tests, with comparison to rigid-rod, eroding-rod, and revised-methodology calculations, for (a) residual rod length and (b) penetration and residual velocity.	22
Figure 11. Data for Interply Series tests, with comparison to revised-methodology calculation, for (a) residual rod length and (b) residual velocity.	23
Figure 12. Datum for Semi-Infinite Series II test, with comparison to rigid-rod, eroding-rod, and revised-methodology calculations, for (a) residual rod length and (b) penetration (note: revised-methodology calculation shown for two values of parameter ΔL_{CRIT}).	24
Figure 13. Rod-deformation-to-erosion-onset model parameter, $\Delta L_{\text{CRIT}}/D_0$, shown as a function of target resistance, for the Al alloys modeled in the current test series, with anticipated interpolation and extrapolation to other Al alloys.	25
Figure 14. Penetration and residual-velocity data for Semi-Infinite Series I tests, with comparison to FZ-model results, for rigid and eroding rods.	27
Figure 15. Data for Finite-Target Series tests, with comparison to FZ-rigid-model and FZ-eroding-model calculations, for (a) residual rod length and (b) residual velocity.	28
Figure 16. Data for Interply Series tests, with comparison to FZ-rigid-model and FZ-eroding-model calculations, for (a) residual rod length and (b) residual velocity.	28

Figure 17. Penetration datum for Semi-Infinite Series II test, with comparison to FZ-model results, for rigid and eroding rods.	29
Figure 18. Penetration and residual-velocity data for Semi-Infinite Series I tests, with comparison to FZ-model results, for rigid and eroding rods and FZ-S model with soft target surface.	30
Figure 19. Data for Finite Target Series tests, with comparison to FZ-S (soft surface) model calculations, for (a) residual rod length and (b) residual velocity.	31
Figure 20. Data for Interply Series tests, with comparison to FZ-S (soft surface) model calculations, for (a) residual rod length and (b) residual velocity.	31
Figure 21. Target resistance and axial rod stress, through the depth of the Finite Target Series target at 1250 m/s striking velocity, as characterized by (a) the FZ-S (soft surface) model and (b) the revised model.	32
Figure 22. Target resistance and axial rod stress, through the depth of the Finite Target Series target at 1000 m/s striking velocity, as characterized by the FZ-S/I (soft surface and interfaces) model.	32

List of Tables

Table 1. Target descriptions for experimental series.	4
Table 2. Ballistic results for experimental series.	5
Table 3. Model properties for target materials.	6

INTENTIONALLY LEFT BLANK.

1. Introduction

The subject of this report is the ballistic interactions of rod and target in the vicinity of the rod-erosion threshold velocity. Its scope is both experimental and analytical. Recently, the author (1) detailed the results of several interesting ballistic tests that straddled the rod-erosion threshold velocity for the case of hemispherical-nosed tungsten-alloy (WA) rods onto thick aluminum (Al)-5083 targets. This report extends that work with added testing and analysis of several different target configurations, including several materials. As a result of incorporating these additional data into the analysis, the understanding of the phenomenology of hemispherical-nosed WA penetration near the erosion-threshold velocity into Al is extended and refined.

The analysis of the tests was performed with a one-dimensional (1-D) penetration model, developed by the author as an extension to a model by Frank and Zook (2, 3). The current model (4, 5) extends the Frank-Zook (FZ) model primarily by incorporating aspects of a theory by Walker and Anderson (6) and adapting them for use in a multiply target configuration. Both models get their pedigree from original penetration theories by Tate (7) and Alekseevskii (8). In response to analysis of the currently presented data, further model revisions are offered to help address the specific issues of deforming, yet noneroding, penetration and erosion transition. Comparison with the current model and experimental data is offered as well, against the FZ model (2, 3), on which the current model's development was based.

The literature (9–17) has long noted a disparity of penetration capability in the vicinity of the erosion threshold. This disparity appears to be very nose-shape dependent. While conical-nosed penetrators appear to gain performance from the altered flow field around the sharp vis-à-vis a blunt tip (10, 12, 13, 17), both conical- and ogival-nosed penetrators have been observed to penetrate above the erosion threshold with a detached, embedded rod tip (10, 12, 13, 16, 17). Below the erosion threshold, both ogival- and hemispherical-nosed rods can exhibit a fascinating form of noneroding behavior in which the rod nonetheless deforms, but conforms to the cavity profile (1, 14–16). In addition to experimental observation, hydrocode analysis has been brought to bear on the problem (14–18).

In recent work involving hemispherical-nosed WA penetrators onto Al targets (1), the author was able to experimentally validate, from post-mortem recovery of test materials, that the leading end of the noneroding rod, in fact, deformed by expanding in diameter >6%. More importantly, it was experimentally determined that the lateral conformance of rod material to target material during the course of this noneroding penetration constitutes an interference fit between rod and target. Based on this very limited experimental result, it was hypothesized that the lateral resistance developed as a result of this interference, and in accordance with plasticity considerations like the Tresca yielding condition, permits an augmentation of the axial stress that the rod can bring to bear upon the rod/target interface. In such a manner, the deforming-yet-

constrained rod is able to penetrate *as if* it were a much stronger rigid rod. In the case reported (figure 1), the “apparent” or effective strength exhibited by the noneroding rod was roughly triple the rod’s intrinsic material strength. According to the hypothesis, it is this effective rod strength that produces this penetration-performance dislocation across the rod-erosion threshold because, following the onset of erosion, this lateral confinement and the resultant axial-stress augmentation is kinematically removed by the flow of the erosion products. In addressing this type of noneroding, yet deforming, penetration, similarities are shared with traditional rigid-body-penetration modeling (19–23); nonetheless, the modeling is made distinct, by way of the rod’s deformation and the nature of the rod/target interference fit. It should be noted that this noneroding yet deforming, circumstance is somewhat analogous (in reverse) to the ballistic phenomenon known as “penetrator dwell,” in which the target deforms and may yield (or fracture), but does not ballistically erode.

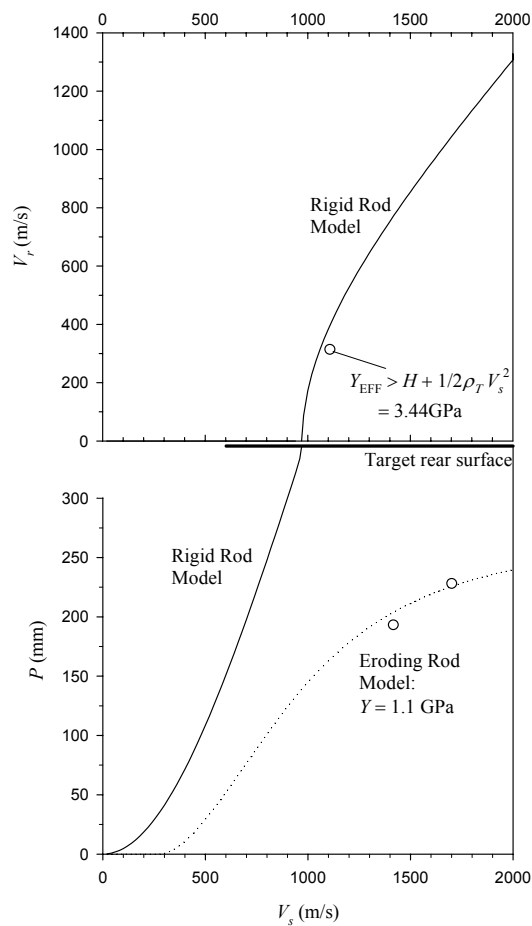


Figure 1. Penetration and residual-velocity data into 344 mm monolithic Al (BHN 97). For comparison, model results for rigid and eroding rods are included.

Forrestal and Piekutowski (24) presented much data that can be used to support the subsequent hypothesis by this author (1). In Forrestal and Piekutowski's work, 6061-T6511 Al targets are penetrated by hemispherical-nosed steel rods of hardnesses R_C 36.6, 39.5, and 46.2. While the recently reported work of the author (1) employed WA rods, both rod hardness and target hardness were comparable to that employed by Forrestal and Piekutowski. To model their data, they use an eroding model above the erosion threshold and a rigid model below it in order to recreate the observed penetration discontinuity at the threshold. This approach was also employed by the author, albeit with a simpler model for rigid penetration, as opposed to the Forrestal model. Finally, like the author, who noted a bulging rod diameter in the noneroding penetrator, Forrestal and Piekutowski also note (with radiography of rods embedded in targets) significant rod-bulging deformities below the erosion threshold, which is to say, among those data for which rigid-body modeling was applied. No hypotheses are, however, offered by Forrestal and Piekutowski as to how and why a significantly deforming rod should be treated as "rigid" in an analysis, and more importantly, the kinematic justification for why such a rod fails to erode in the first place.

Earlier work of Piekutowski *et al.* (25) using nearly identical materials, but ogival instead of hemispherical rods, demonstrates (as have many other authors) the dependence of the transition phenomenon on rod-nose shape. There, the transition to deforming and subsequent rod erosion was only observed at significantly higher striking velocities.

Regardless of nose-shape influence on the process, the crux of the issue is this: the stagnation pressure ($1/2\rho U^2$) from penetrating Al at 1100 m/s is 1.6 GPa. Adding to that, the target resistance of the particular Al alloy (even accounting for variation in what might constitute an appropriate resistance) invariably places the axial stress level at the rod/target interface well beyond the yield strength of an R_C 40 penetrator. These configurations, for hemispherical-nosed rods, are nonetheless observed by many researchers (1, 14–16, 24) to penetrate in a noneroding fashion. The primary contribution of the recent work (1) is in establishing a kinematic hypothesis to explain this discrepancy: that the target's lateral interference against the deforming rod both inhibits the rod erosion while permitting a significantly elevated axial stress to be brought to bear by the projectile upon the rod/target interface. The notion of erosion being inhibited by lateral target interference is not novel, but was posited by Wijk (26), though in that case only as specifically pertains to the final stages of so-called afterflow penetration. No mention is made there, however, of an elevated axial stress that might accompany this lateral confinement and aid the penetration efficiency.

2. Observations

In the present study, the ballistic threat consisted of a hemispherical-nosed WA rod of the following characteristics: 65 g, length-to-diameter (L/D) ratio of 15, a content of 93% tungsten

(W) and 6.3% Nickel (Ni), and swaged (reduced in cross-sectional area) 8%. Because of available supply, there were actually two variations of WA rod employed: one with the remaining 0.7% composition of iron (Fe) and the other of cobalt (Co). Nonetheless, these two rod variations share nearly identical properties, and because all ballistic engagements were at normal incidence, influence due to any variation in, *e.g.*, fracture properties, was minimal. The W-Ni-Fe rods had a nominal Rockwell hardness of R_C 37, with nominal dimensions of 101.9 long \times 6.79 mm diameter, while the W-Ni-Co rods had a nominal hardness of R_C 37.5, with nominal dimensions of 101.7 long \times 6.78 mm diameter. The dimensions and mass of the rods yield a penetrator density of $\sim 17,600 \text{ kg/m}^3$. A hardness of R_C 37 correlates roughly with a strength of 1.1 GPa. The W-Ni-Fe rods were used exclusively in the test series dubbed “Semi-Infinite” and “Finite-Target,” while the W-Ni-Co rods were used exclusively in the test series dubbed “Interply.” Several of the Semi-Infinite Series test results were reported on in the preceding report (1). The target descriptions for the various test series discussed in this report are provided in table 1. All target elements were square or rectangular in shape, between 200- and 305-mm on a side, in length. Because the pedigree of all target plates was not known or available, Brinell hardness testing was done in all cases to provide estimates of material strength properties. These hardness data are incorporated into the targets’ functional descriptions in table 1. While the so-called Semi-Infinite Series targets (which are, nonetheless, finite stacks of Al block) were intended purely as a baseline, it may be noted from table 1 that both the Finite-Target and Interply test series each have two variations on their target “recipe,” respectively.

Table 1. Target descriptions for experimental series.

Rod Employed	Nominal Target Description	Functional Target Description ^a
Semi-Infinite Series I		
W-Ni-Fe	6 \times 2.25 in Al 5083	344 mm Al BHN 97
Semi-Infinite (Single Datum) II		
W-Ni-Fe	7 \times 2 in Al	362 mm Al BHN 190
Finite-Target Series (Without Backing)		
W-Ni-Fe	2 \times 1.3 in Al 5083	65.5 mm Al BHN 97
	1.25 in Al 5083	32.0 mm Al BHN 99
	1.75 in Al 5083	45.2 mm Al BHN 112
Finite-Target Series (With Backing)		
W-Ni-Fe	2 \times 1.3 in Al 5083	65.5 mm Al BHN 97
	1.25 in Al 5083	32.0 mm Al BHN 99
	1.75 in Al 5083	45.2 mm Al BHN 112
	0.0625 in stainless 304	1.58 mm steel R_B 80.2 (\sim BHN 72)
Interply Series (Without Interply)		
W-Ni-Co	5 \times 0.5 in Al 7079 (?)	63.5 mm Al BHN 143
	2 \times 1.75 in Al 5083	90.4 mm Al BHN 112
	0.375 in high-hard steel	9.5 mm steel BHN 512
Interply Series (With Interply)		
W-Ni-Co	5 \times 0.5 in Al 7079 (?)	63.5 mm Al BHN 143
	2 \times 1.75 in Al 5083	90.4 mm Al BHN 112
	0.1 in acrylic	2.54 mm Acrylic
	0.375 in high-hard steel	9.5 mm steel BHN 512

^a Target hardness specified in Brinell hardness number (BHN) or Rockwell B (R_B) scales.

The ballistic results for the test series are given in table 2. There were a total of four tests in the Semi-Infinite Series, 10 in the Finite-Target Series (5 each with and without a thin-steel backing) and 20 in the Interply Series (10 each with and without the Plexiglas interply).

Table 2. Ballistic results for experimental series.

Experiment Designation	V _s (m/s)	V _r (m/s)	P (mm)	L _r (mm)	Comments
Semi-Infinite Series I					
MV1	1108	314	344.0	81+	Perforation, noneroding, rod tail missing
MV3	1416	—	193.2	14	—
MV2	1701	—	228.1	12	—
Semi-Infinite (Single Datum) II					
MV4	1413	—	130.4	~0–3	—
Finite-Target Series (Without Backing)					
MV7	916	696	—	57.1+	Noneroding, rod tail missing
MV5	1055	540	—	26.3+	High yaw, noneroding(?), rod tail missing
MV16	1196	892	—	62.5	—
MV28	1394	1077	—	48.6	—
MV22	1628	1310	—	33.3	—
Finite-Target Series (With Backing)					
MV10	906	593	—	60.1+	Noneroding, rod tail missing
MV14	1053	776	—	57.8+	Noneroding, rod tail missing
MV19	1197	934	—	80.3	—
MV31	1384	1035	—	50.8	—
MV25	1595	1217	—	40.9	—
Interply Series (Without Interply)					
MV24	1251	488	—	~0	Test at ballistic limit, small residual debris
MV15	1300	294+	—	—	V _r is debris (rod exited from film laterally)
MV8	1351	791	—	18.5	—
MV37	1391	588	—	8.5	—
MV11	1455	1015	—	37.8	—
MV43	1521	934	—	30.1	—
MV30	1536	841	—	20.8	—
MV45	1625	1198	—	25.5	—
MV34	1641	1039	—	21.6	—
MV40	1722	1184	—	20.1	—
Interply Series (With Interply)					
MV21	1261	0	—	—	Bulge in rear plate, near ballistic limit
MV12	1281	570	—	30.9	—
MV39	1360	801	—	28.6	—
MV18	1381	801	—	27.0	—
MV42	1455	848	—	28.5	—
MV27	?	415	—	21.6	X-rays not triggered, no V _s obtained
MV46	1501	779	—	19.3	Redo of MV27
MV44	1547	972	—	21.6	—
MV33	1597	905	—	20.1	—
MV36	1708	1128	—	14.7	—

3. Modeling

From these and other data were deduced the targets' material properties that would be employed in the penetration model. These properties are given in table 3 and include density (ρ_T), elastic modulus (E), yield and ultimate strengths (σ), and resultant target resistance (H). For the softer alloys of Al, the properties are drawn from handbook alloys of comparable hardness. For the hard Al and the steels, hardness conversion tables were used. The acrylic strength, being highly rate dependent, was estimated from scant data. The target resistance was calculated from Tate's formula, except that ultimate rather than yield strength was employed therein. This formula takes the following form:

$$H = \sigma \left[\frac{2}{3} + \ln \left(\frac{2E}{3\sigma} \right) \right]. \quad (1)$$

Table 3. Model properties for target materials.

Material	ρ_T (kg/m ³)	E (GPa)	σ_Y (GPa)	σ_{ULT} (GPa)	H (GPa)
Al BHN 97	2700	75	0.276	0.310	1.78
Al BHN 99	2700	75	0.276	0.310	1.78
Al BHN 112	2700	75	0.345	0.372	2.07
Al BHN 143	2700	75	0.476	0.531	2.77
Al BHN 190	2700	75	—	0.627	3.16
Steel R _B 80.2 (~BHN 150)	7850	205	—	0.496	3.12
Steel BHN 512	7850	205	—	1.896	9.38
Acrylic	1190	2.55	0.14 (est.)	0.235 (est.)	0.62

In all cases, a material's spall resistance, used to characterize a target material's resistance in the limit as a free surface is approached, has been characterized by the value $H/3$. Because the rod's hemispherical nose shape is blunt, all Bernoulli shape factors, k_R and k_T , are retained at a value of 0.5. The plastic zone extent (PZE) for all materials is retained at a model-default value of 3.5 rod diameters. The PZE, an estimated quantity, represents the size, in rod diameters, that the plastic zone extends in front of and away from the moving rod/target interface (4, 5). Any target plies entrained in this plastic zone impart a contribution to the aggregated density and resistance of the target, as instantaneously perceived by the rod. Results are somewhat insensitive to changes in the value of PZE, unless it is made small enough to approach the lower limit of zero.

The target recipe variations within a test series that are described in table 1, while designed to have minimal ballistic influence, were intended to challenge the model's ability to not over- or under-compensate for the influence of target layers with significantly disparate material

properties. This challenge to modeling accuracy can be traced to the manner in which multiple plies are treated within a target and have been demonstrated (5) with several earlier penetration models. For example, both the original Tate (7) and the FZ (2, 3) models suffer this problem in different circumstances and to different extents, due to the inability (in the case of Tate's) or the limited ability (in the case of FZ) to "look ahead" of the rod/target interface and ascertain the influence of upcoming density and resistance dislocations (i.e., target interfaces) upon the target's instantaneous resistance.

The testing program was originally designed for this (now secondary) purpose of validating the modeling algorithm for multi-ply target laminates. The much larger experimental effect actually observed and the concomitant modeling challenge, not appreciated at program outset, was in understanding the modeling ramifications of noneroding, yet deforming, penetration, and any associated transitions to a fully eroding configuration.

The preceding report (1) began this process of modeling noneroding, yet deforming, penetration as it pertains to hemispherical-nosed rods into thick monolithic targets (Al-5083). It hypothesized the stress field and kinematic behavior of rod deformation to be compatible with Magness and Scheffler's qualitative description of the event for ogival-nosed rods (16), Forrestal and Piekutowski's experimental observations (24), as well as the post-mortem data from the current Semi-Infinite Series of tests. Under the hypothesized behavior, the lateral contact between rod and crater, established during penetration, takes the form of an interference fit. The resulting lateral stress, H_{LAT} , established by this interference fit permits, in accordance with the Tresca yield condition, the axial stress in the rod to exceed the rod's yield strength, Y , taking on an value equal to $Y + H_{LAT}$ (figure 2). With a low enough striking velocity, V_s , this augmented axial stress (an "effective" rod strength, as it were) is sufficient to deter rod erosion, with noneroding penetration as the result.

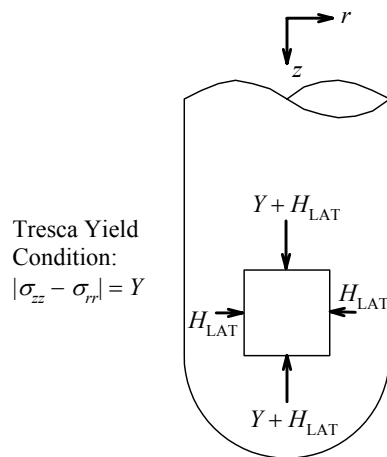


Figure 2. Schematic showing how lateral confinement may augment the axial stress brought to bear by the rod, in light of plastic yield condition.

A primary effect of this stress augmentation, in modeling the problem, is the revision of the extended Bernoulli equation. Solved as part of the penetration analysis, this equation balances the stress across the rod/target interface by considering the stagnation effects of both the eroding rod and eroding target. As pointed out by Segletes and Walters (27), the axial stress term given by Y in the equation actually arises from a σ_{zz} stress term, where z is the axial coordinate. When the stress is uniaxial, σ_{zz} is limited to the yield strength, Y . However, for the multiaxial condition described by figure 2, the axial stress component will rise above the uniaxial strength to an “effective strength” value, Y_{EFF} , equal to $Y + H_{\text{LAT}}$. In its simplest (slender-rod assumption) form, the extended Bernoulli equation becomes

$$k_R \rho_R (V - U)^2 + Y_{\text{EFF}} = k_T \rho_T U^2 + H . \quad (2)$$

The observed dislocation in penetration-vs.-striking velocity curve is then a direct result of the reduction of Y_{EFF} from $Y + H_{\text{LAT}}$ back to Y , following the onset of eroding penetration and the concomitant loss of lateral interference with the target wall.

While the preceding report (1) estimated the H_{LAT} value necessary to retain rod rigidity for one datum striking at 1108 m/s, it did not establish a general rule or methodology that would permit one to calculate or estimate the conditions under which the erosion transition might commence. Furthermore, based solely on the limited test results into 344 mm thick monolithic Al-5083 (BHN 97), as shown in figure 1, one might be tempted to infer from the preceding report that this erosion threshold is a function of striking velocity alone, so that once above the erosion-threshold striking velocity, classical eroding penetration is the immediate result from the impact outset. If such an assumption has merit, then one should expect that ballistic data would fall either upon the curve modeled as noneroding (with effective strength $H_{\text{LAT}} + Y$), or upon that modeled as fully eroding (with strength Y), as it does in figure 1.

However, the data from the other test series prove more complicated than this simple assumption allows. Figure 3a shows residual-length-vs.-striking velocity for the so-called Finite-Target Series of tests, along with rigid-rod and eroding-rod predictions. In this figure, one may observe that the experimentally observed residual length transitions from the noneroding value to the fully eroding curve, not abruptly, but over a 500 m/s striking-velocity range from roughly 1100 to 1600 m/s. The residual-length data at striking velocities below 1100 m/s were measured at less than the original rod length. However, this was not because of erosion, but rather because of rod fracture in which the tail of the rod remained entrained in the target at the moment of radiography, due to lateral interference with the target. The leading edge of the rod, observed from radiography, clearly retained its original hemispherical-nosed shape, leading to the conclusion that these rods were, in fact, noneroding. Further, the fractured midsection of these rods was clearly observable, further confirming that the missing rod length was from the tail, rather than the tip of the rod (figure 4). In any event, the notion that the erosion transition is governed solely by the striking velocity is wholly dispelled by figure 3a.

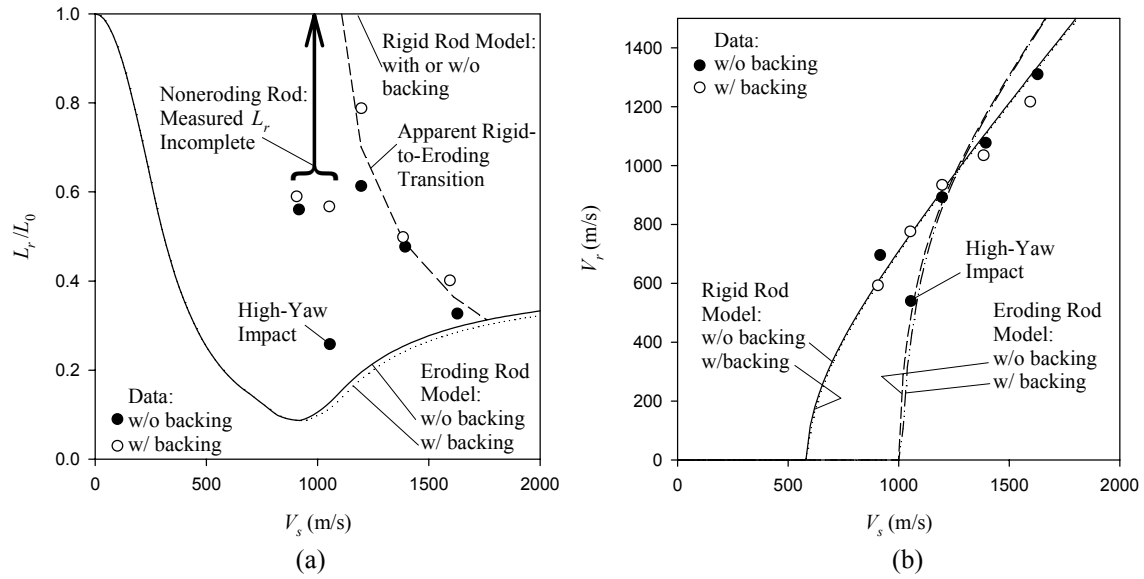


Figure 3. Data for Finite-Target Series tests, with comparison to rigid-model and eroding-model calculations, for (a) residual rod length and (b) residual velocity.

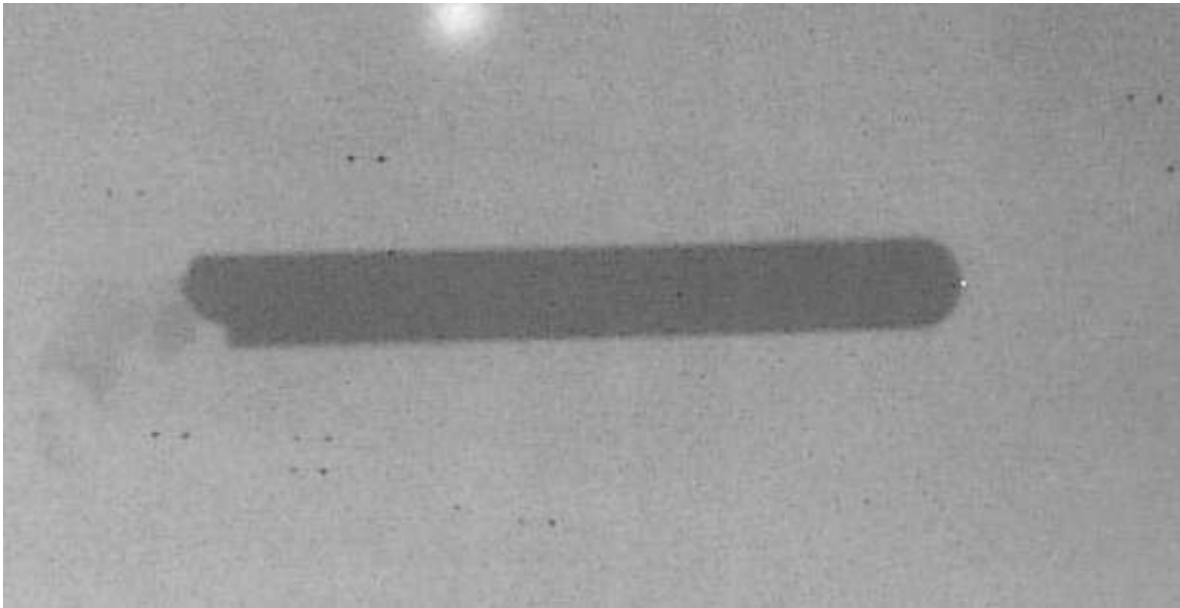


Figure 4. Radiographic image of residual rod from test MV7, depicting intact nose and fractured tail (note: rod is moving left to right on image).

The results for the Interply Series of tests, given in figures 5a and 5b, prove equally disappointing when the tests are modeled as purely rigid or purely eroding. These results reinforce the conclusion that the simple interpretation, defining the penetration mode as a function of striking velocity alone, is not sufficient to describe the phenomenon of erosion transition.

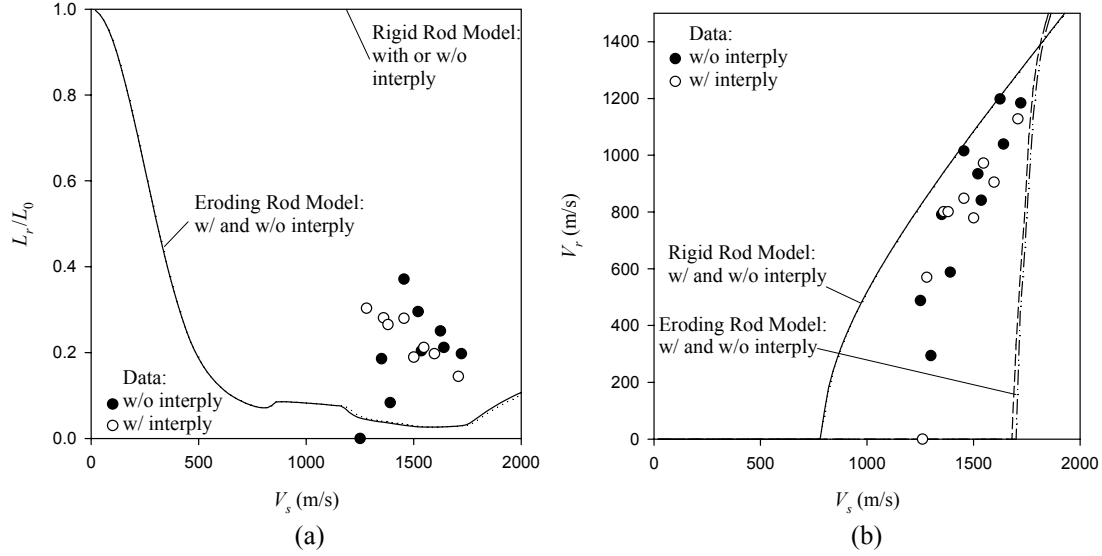


Figure 5. Data for Interply Series tests, with comparison to rigid-model and eroding-model calculations, for (a) residual rod length and (b) residual velocity.

A further deficiency may be noted in figure 3b, which depicts the experimental and predicted residual velocities resulting from the Finite-Target Series. Below 1100 m/s, the data are captured well by the rigid-rod curve, as is expected. However, for the higher striking velocities, not only does the eroding-rod curve overestimate the residual velocities, but the rigid-rod curve does as well. This is disconcerting, as one would, in any event, expect the data to fall between the two curves. We will endeavor to address this issue later (see subsection 3.3 entitled “Impact Pressure”). Consider first, however, the issue of the residual length discrepancy noted in figure 3a and its implications for the erosion trigger.

3.1 Trigger for Erosion

Figure 3a makes clear that the erosion transition is not triggered by impact velocity alone. There are many ways to attempt to address this issue. The simplest, and one first tried, is to assume that the specific manner of the rod/target interference fit (and thus the lateral resistance, H_{LAT}) is a function of the striking velocity. In this manner, an effective yield strength may be back-calculated, as a function of striking velocity, in order to match the experimentally observed residual lengths from the Finite-Target Series. Figure 6 shows the result of such a back-calculation for $Y_{EFF} = Y + H_{LAT}$. For striking velocities lower than 1108 m/s, the Semi-Infinite Series test datum had indicated that noneroding penetration would result, and so the rod’s minimum effective strength is governed by the parabolic relation derived from the rigid-penetration stress balance, $Y_{EFF} = H + 1/2\rho_r V_s^2$. The back-calculated effective strength covers the striking velocity range between 1108 and 1760 m/s. Per figure 6, the back-calculations represent an averaged effective yield strength for the rod (i.e., exerted over the full event duration), in order to produce the residual lengths noted in the rigid-to-eroding transition of figure 3a.

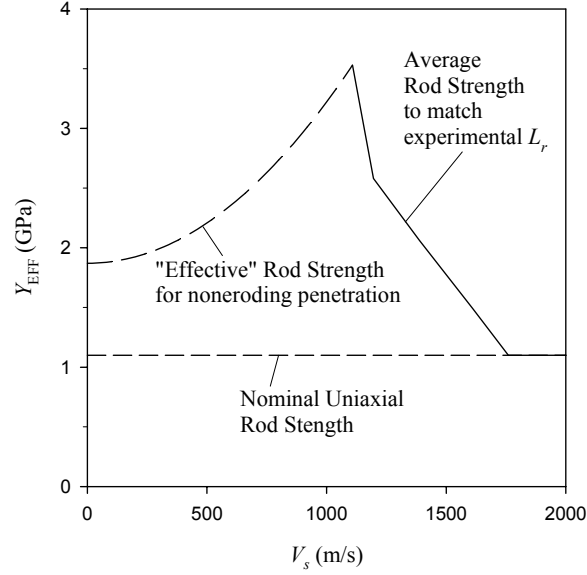


Figure 6. Back-calculated “effective” velocity-dependent rod strength, to accurately model residual length in Finite-Target Series tests, assuming effective strength was to act over full duration of ballistic event.

However, this approach can only have merit if it can be used to accurately predict results from other test series beyond the Finite-Target Series. But, in fact, such an approach does a very poor job if applied to, for example, the Semi-Infinite Series of tests, and severely overpredicts ballistic performance into monolithic Al for striking velocities covered by the back-fit (i.e., between 1108 and 1760 m/s). The logical conclusion is that H_{LAT} cannot be solely a function of V_s . A more likely scenario is that H_{LAT} is a material parameter and no more an intrinsic function of striking velocity than is the target resistance, H , itself. Considering H_{LAT} fixed for a given material, the remaining possibility to explain the data is that the transition from noneroding to eroding occurs at some point during the course of the ballistic event so that, at some intermediate stage, the effective rod strength transitions from a value of $H_{LAT} + Y$ to the nominal value of Y . Under such a hypothesis, the principal modeling issue becomes the trigger that precipitates the erosion transition.

One may effectively rule out elapsed time as the erosion trigger (i.e., the trigger to remove lateral interference from the target), as it would allow, without limit, for progressively greater depth of noneroding penetration as the striking velocity was progressively raised. One may also rule out penetration depth as the erosion trigger, as this would imply, regardless of striking velocity, that all impacts would achieve the noneroding penetration to the same depth before commencing erosion. Such a notion is incompatible with the Semi-Infinite Series data of figure 1.

Consider then the possibility that erosion is triggered by a change in rod length; call it ΔL_{CRIT} . While it is normal, in the context of penetration mechanics, to consider any change in rod length

to be precipitated by and following the onset of rod erosion, it is known in the current context that the noneroding penetration is accompanied by rod deformation. Forrestal and Piekutowski (24) observed this fact definitively. In the current study, the noneroding datum from the Semi-Infinite Series ($V_s = 1108$ m/s) experienced a 6% diameter increase over at least the leading 25 mm of rod (1) (figure 7). Continuity dictates for that portion of the rod experiencing a 6% diameter increase that the length decreases by 11%. Depending on what portion of the overall rod length (original length of 101.9 mm) experienced this diameter expansion, the rod diminished somewhere between 3% and 11% of its overall length without the onset of erosion.



Figure 7. Photograph depicting residual-rod fragment recovered from test MV1. While rod tip appears undeformed, measurement reveals a 6% increase in rod diameter.

Thus, it seems quite feasible that the amount of noneroded rod foreshortening, ΔL_{CRIT} , being indicative in some way of lateral rod strain or perhaps of irreversible nose-geometry deformation, be the principal factor to govern the onset of erosion. The observed phenomenology is, at casual glance, compatible with this explanation. For if the striking velocity is small enough that the noneroding deformation remains limited, the penetration may wholly proceed through the target in a noneroding manner. If, on the other hand, the stagnation pressure from a high striking velocity is large enough to overwhelm the augmentation of axial stress by a value H_{LAT} , then the noneroding phase of the event will quickly pass with the rapid rod deformation, and the eroding phase will dominate the event.

The challenge to understanding this phenomenon in general will be the fact that the tendency to establish an eroding flow field is a function of many factors, at a minimum including rod material, target material, and most importantly, the rod's nose geometry. In the current test series, both rod material (WA) and the rod's nose geometry (hemispherical) vary negligibly. And for the target material (Al) where this phenomenon might be anticipated, the density is constant, and only the target resistance varies with the particular alloy. It is possible that impact

velocity will play a limited role, but only at striking velocities higher than those examined in this study. For as the striking velocity is increased toward the hydrodynamic range, with the concomitant increase in target-crater size, a point will be reached where the crater size grows large enough to preclude the lateral interference between rod and target. When this happens, ΔL_{CRIT} will necessarily diminish to zero. But in the present study, striking-velocity dependence will not be reflected in the modeling of ΔL_{CRIT} . Thus, it is hoped that for the purposes of modeling the erosion transition for these test series, the foreshortening-to-erosion-onset parameter, ΔL_{CRIT} , may be solely correlated with the target alloy's resistance to penetration, H .

In this regard, there are two limiting cases to look to for guidance. For a target with vanishingly small resistance, one would expect a negligible phase of interference fit between rod and target because there is nothing but inertia to resist the lateral expansion of the target. At the other extreme, one of very large target resistance, one would also expect a negligible phase of interference fit with the target because a very hard target would quickly force the rod into an erosive flow field configuration, before an embedded interference fit could even be established. There would thus appear to be only a limited range of intermediate target hardness at which this unique interference fit might reasonably be established. This correlation will be sought, once the remaining modeling groundwork is established.

3.2 H_{LAT} Magnitude

In the preceding report (1), the magnitude of H_{LAT} was estimated so as to provide for a fully rigid-body penetration for the $V_s = 1108$ m/s datum. Requiring rigidity necessitated the use of an H_{LAT} value $1.31 \times$ the target's penetration resistance. The experimental datum was, however, not fully rigid, as the recovered rod fragment was observed to have expanded 6% in rod diameter during the course of the penetration. This is one reason to believe the actual value of H_{LAT} to be less than this 1.31 value. While one might expect the resistance-to-radial crater expansion to be of a similar magnitude to the resistance-to-axial penetration, there is reason to suspect that the two values are not identical. For example, the classical indentation literature (28) indicates that both steel and Al's resistance to deep indentation (penetration) is from 2.8 to $3 \times$ the yield strength, while the derived expressions presented by others (29–31) for spherical cavity expansion can range from 3.5 to $4.1 \times$ the yield strength, depending on material stiffness and strength for the range of steels and alloys of Al in the current study. On this basis, one might expect the ratio H_{LAT}/H to lie in the range of 1.17 to 1.46. In the end, an empirically selected value of $H_{\text{LAT}} = 1.22H$ proved effective, as will be shown.

3.3 Impact Pressure

The rod deceleration equation, for the traditional case, is given by

$$\dot{V} = -\frac{\sigma}{\rho_R(L-s)}, \quad (3)$$

where V is the rod velocity, σ is the decelerative stress applied at the elastic-plastic boundary in the rod or, in the case of a rigid body penetrator, the stress applied at the rod's nose, ρ_R is the rod's density; L is the rod length, and s is the size of the small plastic zone at the leading edge of the rod. In Tate's original derivation (7), a slender rod is assumed so that s is a negligibly small fraction of L . In the case of an eroding rod, the rod's strength limits the stress that composes the decelerative force, and thus $\sigma = Y$. In the case of rigid penetration, there is no plastic zone, so that $s = 0$. Further, the target's resistance plus the inertial pressure of the target's stagnation flow upon the penetrator tip, being $< Y$, composes the decelerative stress. Thus, $\sigma = H + k_T \rho_T U^2$ represents the decelerative stress for rigid-body deceleration in the traditional case.

The issue was raised in reference to figure 3b that the modeled residual velocity from the Finite-Target Series was too large, falling above the data in both the case of eroding-rod and rigid-rod modeling. The implication is that the actual deceleration of the rod is larger than that being modeled. Because the eroding and rigid models should straddle the experimental data, one would have to account for a greater decelerative stress in the rigid-penetration case, beyond $\sigma = H + k_T \rho_T U^2$, in order to achieve this goal. While raising the target resistance is a simple and direct way of increasing this decelerative force on the rigid rod, it suffers the same flaw as modeling the erosion transition with a velocity-dependent target resistance; namely, it substantially worsens the modeling predictions for the Semi-Infinite Series.

If the resolution does not come by way of target resistance, then the stagnation pressure is the only other quantity at hand. The pressure term in the rigid-body deceleration equation is $k_T \rho_T U^2$. While the Bernoulli pressure is more than just a steady-state pressure, it nonetheless does not account for any wave mechanics in the flow field. At the moment of actual impact, however, the transient impact pressure, given by $\rho_T U_s u_p$ (U_s is the shock-wave velocity and u_p is the particle velocity behind the shock wave), can be more than an order of magnitude larger than the Bernoulli pressure. The calculation of this impact pressure requires the knowledge of several additional material parameters for the rod and target, namely the bulk sound speed C_0 and the empirically derived slope of the shock-vs.-particle velocity curve, given by S . These values are widely published equation-of-state parameters, available for a wide variety of materials.

With such a large disparity between Bernoulli and transient shock pressures, the much larger shock pressure need not act long in order for it to have a measurable effect on the decelerative impulse imparted to the rigid-rod. And while the reality is that this large transient pulse decays rapidly to the Bernoulli pressure value, the implementation chosen here, for simplicity, is a step function. The full impact stress is arbitrarily applied for a duration equal to the time required for a rarefaction (stress-release) wave to traverse the rod diameter three times, *i.e.*, an impact pressure differential ΔP is added to the Bernoulli stress during the period of time $t < 3D_0/C_0$ (note that a Poisson's ratio of 1/3 has been assumed, making the longitudinal wave speed of the release wave equal to the bulk sound speed C_0). In the current context of a 6.79 mm WA rod ($C_0 = 4030$ m/s), this translates to ΔP being applied for a duration of ~ 5 μ s.

Note that this pressure differential, while present, does not affect the Bernoulli balance of equation 2 between rod and target (which governs the relation of U and V), because this elevated impact pressure is present in both rod and target, thus canceling on balance. Rather, this pressure differential serves to bolster the driving stress, σ , for rigid-rod deceleration (equation 3). This pressure differential will also play a role in the deceleration of deforming, yet noneroding, rods, to which this report presently addresses itself.

3.4 Plastic Zone Size in Rod

3.4.1 Equation of Noneroding Rod Motion

The equation that governs the decelerative motion of a penetrating rod was given as equation 3, valid for the cases when the penetrator is an eroding or a purely rigid rod. A vital question to ask is how this governing relation may be altered in the current context, where the rod is neither eroding nor purely rigid. In the case of a rigid rod, the issue is that the decelerating stress on the rod's elastic nose is below the magnitude of the rod's strength; nonetheless, its value is still obtainable from consideration of the target's flow around the rigid rod. For eroding rods, however, the issue differs. Traditional methodology, espoused by all from Tate (7) to Walker and Anderson (6), is to consider only the elastic portion of the rod in the control volume used to derive the rod-deceleration (i.e., momentum) equation. The reason for so doing is threefold: (1) because the axial stress magnitude at the elastic/plastic boundary is accurately known to be the rod's strength, (2) it avoids the need to calculate the radial stress gradient in the erosion zone, and (3) it avoids the need to tabulate the momentum efflux from the products of rod erosion, the velocity of which have changed not only in their magnitude, but also their direction of flow. These gradient and flux terms, difficult to estimate, would become an important part of the momentum equation, were the eroding rod tip considered as part of the control volume.

The problem with adopting this traditional methodology to the present case of deforming, yet noneroding, penetration is in accurately ascertaining the time-dependent location, s , of the elastic/plastic interface from the rod's nose. In the case of a traditionally eroding rod, s may be estimated from the consideration of residual length data in semi-infinite penetration tests. But the plastic zone size in the traditional eroding rod case bears little resemblance to that currently observed in the noneroding tests, nor those noneroding data reported by Forrestal and Piekutowski (24). From the nonrigid form of equation 3, given as

$$\dot{V} = -\frac{Y}{\rho_R(L-s)}, \quad (4)$$

it may be deduced that, as s becomes a significant portion of rod length L , its influence on the deceleration result becomes vital. It has already been established with the recovered noneroding rod fragment from the Semi-Infinite Series of tests (figure 7) that a significant percentage (25% or more) of the noneroding rod becomes plastic, and not just a small zone near the rod tip, as in the case of traditional eroding penetration. The radiographic data of Forrestal and Piekutowski (24) show

upwards of 50% of the uneroded rod within the plastic zone. And yet, no immediate guidance suggests itself as to how to model a time-dependent value of s for the noneroding case.

This quandary suggests that an alternative control volume might prove more profitable. If the complete rod is considered in developing the rod-deceleration equation, the need to know the value of s , in order to solve it, evaporates. Additionally, there is arguably no radial gradient of stresses within, nor efflux of erosion products from, the noneroding rod tip, thereby mitigating a primary difficulty in considering the plastic portion of the rod as part of the control volume for rod deceleration. What is required, however, is knowledge of the velocity and axial stress at the plastic tip of the noneroding rod. The rod-tip velocity is, by definition, U . The differential between velocity V in the elastic portion of the rod and U in the plastic portion leading up to the tip is accommodated by the diameter expansion in the plastic portion of the rod. The axial stress at the tip comports with prior discussions on interference fit between the rod and the target during the noneroding phase, as well as impact pressure considerations. Thus, the rod-deceleration equation becomes in the noneroding phase, in lieu of equation 4,

$$\dot{V} = -\frac{Y + H_{\text{LAT}} + k_R \rho_R (V - U)^2 + \Delta P}{\rho_R L}, \quad (5)$$

where the impact pressure differential ΔP is conditionally applied only during the period of time specified by $t < 3D_0/C_0$. When noneroding penetration ceases and erosion commences, the deceleration equation should revert back to the traditional form of equation 4.

Figure 8 depicts the situation for the case of noneroding penetration. In it, the equations for both viable approaches to rod deceleration are given, alternately requiring knowledge of the stress magnitude at the rod tip, or the size of the noneroding plastic zone, respectively. Equation 5 depicts the former. In the simplest of cases where the penetration is steady (and time-rates of change may be neglected), the Bernoulli stress balance between rod and target is achieved through equating the stresses at locations B and T, as shown in the figure.

3.4.2 Extended Bernoulli Equation

While equation 5 effectively removes the need to know how s behaves for the noneroding case, its behavior for the traditional eroding case still needs to be specified for use in equation 4. Furthermore, while the extended Bernoulli equation 2 for the slender-rod condition is not a function of s , the full extended Bernoulli equation actually solved in the model comports with the analysis of Walker and Anderson (6) to include nonlinear effects, with extensions by the author for laminate targets (4, 5). It is given as

$$\left(k_R - \frac{\dot{s}}{2\dot{L}}\right)\rho_R(V - U)^2 + Y_{\text{EFF}} - \frac{\rho_R s}{2}(\dot{V} + \dot{U}) = k_T \bar{\rho} U^2 + \bar{H} + \frac{X_U \dot{U}}{U} + \frac{X_\alpha \dot{\alpha}}{\alpha} + \frac{X_R \dot{R}}{R}, \quad (6)$$

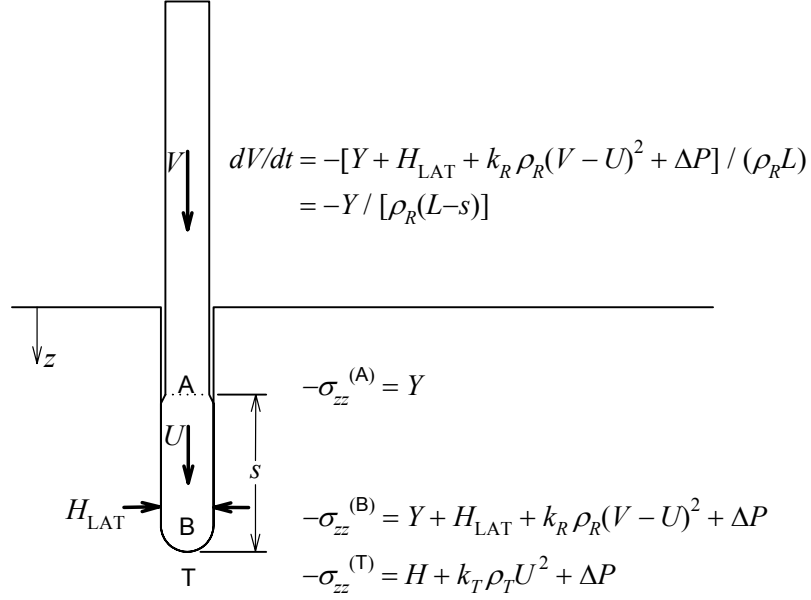


Figure 8. Schematic depicting the axial-stress levels at three locations, A, B, and T along the rod centerline, along with two versions of the rod-deceleration equation (one requiring knowledge of s , the other not).

where $\bar{\rho}$ and \bar{H} are the appropriately aggregated density and resistance in the target's plastic zone, and X_U , X_α , and X_R are aggregated factors from the target's plastic zone associated with the nonsteady effects of penetration rate U , Walker-Anderson's plastic zone size parameter α , and crater radius R , respectively. Equation 6 would seem to require knowledge of s for both the eroding and noneroding cases. Given the presence of time derivatives of s therein, the response of equation 6 can be sensitive to arbitrarily selected forms for s . Therefore extreme care must be taken in its specification. First, consider the case of the traditionally eroding rod, where the presence of s is made known in both equations 4 and 6.

One of the primary benefits in properly accounting for s is in modeling rod deceleration in the final stages of penetration (where L often shrinks to the order of s in magnitude). In the absence of modeling s , the residual rod length is always underestimated, a point that has been noted by many regarding the original Tate model (which assumes $L \gg s$, a valid slender-rod assumption except in the final stages of rod erosion). To handle s for the traditionally eroding case, the current model draws upon and adapts an *ad hoc* algorithm from its FZ model roots (2). The FZ approach chose not to deal with the vagaries of modeling s explicitly, but instead increased Y as a decreasing function of L so as to match the experimental record of residual length. From equation 3, it can be seen that these two approaches are mathematically analogous (*i.e.*, $s/L \approx 1 - Y_0/Y_{\text{FZ}}$) in their effect on rod deceleration. But while the $Y_{\text{FZ}}(L)$ approach remedied the residual length calculation, it did introduce a deleterious effect, in that it forced arbitrarily larger values of target resistance H to be used in compensation for a rod strength function, Y_{FZ} that increased value with rod erosion.

Modeling the effect as a finite plastic zone s instead of a rod-strength effect $Y_{FZ}(L)$ provides a more faithful model of reality and removes grounds for criticism unrelated to the erosion-threshold modeling at hand. Therefore, in lieu of modeling Y as a function of L , a function for s was selected to closely match the dV/dt behavior of the FZ model's $Y_{FZ}(L)$ function at small L , where the influence of s is large. The function to model s , for the case of a traditionally eroding rod, is empirically selected as

$$s = s_{\text{ERODE}} = D_0 \frac{2A}{\pi} \tan^{-1} \left(\frac{\pi}{2A} \left[\frac{L}{D_0} + B \left(\frac{L}{D_0} \right)^3 \right] \right) \text{ (traditionally eroding rod)}, \quad (7)$$

where A and B have both been set to 0.8. This function asymptotes to a constant value of $s = AD_0$ when the rod length is large, and to $s = L$ as the rod length shrinks to zero. The parameter B affects the rate of asymptote. Penetration results with this model revision have been verified to closely follow the FZ model results for semi-infinite penetration, which in turn, match the residual length data for semi-infinite penetration into rolled homogeneous armor (RHA) (2). The time derivative of s , for use in equation 6 is obtained by way of the derivative of s with respect to L , as

$$\frac{\dot{s}}{\dot{L}} = \frac{1 + 3B \left(\frac{L}{D_0} \right)^2}{1 + \left(\frac{\pi}{2A} \left[\frac{L}{D_0} + B \left(\frac{L}{D_0} \right)^3 \right] \right)^2} \text{ (traditionally eroding rod)}. \quad (8)$$

For the deforming, yet noneroding, condition, there is no clear guidance on how s should be formulated. It was for this reason that equation 5 was developed to remove its considerable influence from the rod deceleration equation. But its retention in the extended Bernoulli equation 6 remains. Yet if one hypothesizes a noneroding form for s as a nontrivial perturbation of equation 7, in the form of

$$s = s_{\text{ERODE}} + \delta s \text{ (deforming, noneroding rod)}, \quad (9)$$

where δs is the noneroding augmentation to s , then it is possible to select a reasonable form for δs that has a zero net contribution to the extended Bernoulli equation (equation 6). From the extended Bernoulli equation, it is seen that such a zero-sum form on δs must satisfy the equation

$$\frac{\delta \ddot{s}}{2\dot{L}} \rho_R (V - U)^2 + \frac{\rho_R \delta \dot{s}}{2} (\dot{V} + \dot{U}) = 0. \quad (10)$$

The solution to this equation, in light of the kinematic constraint $dL/dt = -(V - U)$, is

$$\delta s = \delta s_0 \frac{\dot{L}_0}{\dot{L}} \exp\left(-2 \int_{V_0}^V \frac{dV}{\dot{L}}\right). \quad (11)$$

While equation 11, like equation 7 before it, ignores the initial transient creation of the plastic zone s , they both treat the subsequent decay of s as a function of changes in L , dL/dt , and V . As dL/dt approaches zero, the noneroding δs also vanishes, as would be expected. Because the δs form satisfies equation 10, all contributions to the extended Bernoulli equation (equation 6) for nonrigid, noneroding penetration are identical to those arising solely from s_{ERODE} , which at least has the virtue of being fit to data for residual length for semi-infinite penetration data into armor.

So while the proposed form for a noneroding s , given by equation 9 remains *ad hoc* and subject to step-wise dislocations as the penetration mode transitions to and from eroding, noneroding, and/or rigid-body, it nonetheless possesses several virtues. First, it accommodates arbitrarily large values of noneroding s . Second, it does not allow for arbitrary tailoring of results through wanton specification of an s function. Most importantly, however, in conjunction with equation 5, it dispatches the need to know the magnitude of the noneroding s function (*i.e.*, the size of the rod's plastic zone) explicitly in order to solve the governing equations for noneroding penetration.

3.5 Integration of Rod Deformation

It was proposed that the foreshortening-to-erosion-onset parameter, ΔL_{CRIT} , may be respectively correlated with each target alloys' resistance to penetration. An implementation issue, in this regard, is how to tabulate the change in rod length vis-à-vis ΔL_{CRIT} , if the noneroding phase of the penetration traverses target elements of different resistance (each with a unique value of ΔL_{CRIT}).

If one envisions the ΔL_{CRIT} parameter as a measure of the allowable noneroding deformation or damage that the rod may sustain prior to the onset of erosion, then the amount of length change that the rod sustains in any one element must be prorated by that element's ΔL_{CRIT} , in order to ascertain the fractional damage from that element. Thus, define a nondimensional deformation parameter D as

$$D = \sum_{i=1}^n \frac{\Delta L_i}{\Delta L_{\text{CRIT}(i)}}, \quad (12)$$

summed over each target element i of the n successive target elements being penetrated in noneroding fashion. With this definition, noneroding penetration ceases when the value of deformation D reaches unity.

4. Modeling Results

The framework has been laid out by which it is proposed to model the phenomenon of deforming, yet noneroding, penetration, along with its subsequent transition to fully eroding penetration. The basic premise is that, during a perhaps limited phase of noneroding penetration, the rod nonetheless deforms (expanding in diameter and thus shortening in length), but is prevented from eroding because of the prevailing interference fit between rod and target. The duration of this noneroding phase of the penetration is dependent upon a permissible level of rod deformation as measured by ΔL_{CRIT} , which itself is dependent upon rod and target material properties and nose geometry. A method was devised to account for this deformation, should it occur through the course of several target elements, each with its own value of ΔL_{CRIT} .

Equation 2 provides the Bernoulli balance, wherein the effective rod strength, Y_{EFF} , equal to Y in the fully eroding case, becomes $Y + H_{\text{LAT}}$ in the case of noneroding penetration where the rod is laterally constrained by the target wall with a resistance H_{LAT} . The value of H_{LAT} , the lateral target resistance, is surmised to be in the vicinity of a material's axial resistance, H , and is taken as $1.22H$ in the current study.

Further, it is believed that the large impact pressure pulse that occurs during the several microseconds after initial impact provides a notable decelerative impulse to rigid and noneroding rods (above and beyond the Bernoulli pressure) and should not be ignored. Its magnitude may be easily calculated from material-shock properties and, for simplicity, its form is taken as a square wave with a duration of application in the current study set to the time required for a rarefaction (stress-release) wave to traverse the rod diameter three times, such that $t < 3D_0/C_0$. In the current context of $L/D = 15$ WA rods of 101.9 mm length, this duration is $\sim 5 \mu\text{s}$.

While equation 3 provides the archetypal rod-deceleration equation form for both rigid and eroding rods, the complications with using this form for deforming, yet noneroding, rods proves daunting because of the unknown nature of the plastic zone size s . As such, equation 5 was derived as an alternative deceleration equation. Unlike the traditional form, which is derived by considering the forces and momentum in the elastic portion of the rod, equation 5 is solved by considering the forces and momentum in the complete rod, which is not fully elastic. Rather than requiring a time-dependent estimate of the plastic-zone size in the rod, equation 5 instead requires an accurate knowledge of axial stress at the rod's noneroding tip.

Further, a method was devised to allow the extended Bernoulli equation 6, detailing the stress balance across the rod/target interface, to be solved without knowing the magnitude of the nonrigid, noneroding component to s .

With this revised methodology, and the material parameters specified in table 3, the Finite-Target Series of tests, previously modeled in figure 3, were modeled again. A permissible level

of rod deformation, ΔL_{CRIT} , set equal to $1.4D_0$ for the BHN 97 and BHN 99 Al target elements (resistance $H = 1.78$ GPa), was employed to produce the results shown in figure 9. While this value of ΔL_{CRIT} was fitted to the data, its reasonableness is validated by the results of Forrestal and Piekutowski (24), who observed noneroding rod foreshortening of $1.43D_0$ just below the erosion threshold for a very comparable R_C 39.7 hemispherical-nose steel rod into Al-6061-T6511.

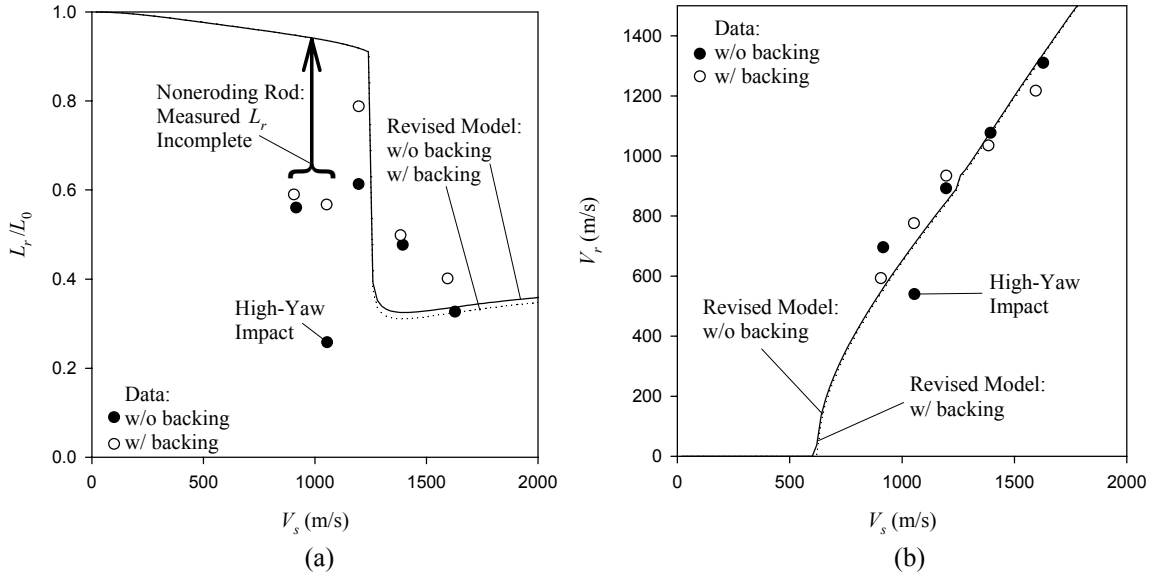


Figure 9. Data for Finite-Target Series tests, with comparison to revised-methodology calculation, for (a) residual rod length and (b) residual velocity.

While the modeled transition from noneroding to fully eroding, as shown in figure 9a is still a bit more sudden than the experimental data reflect, the model nonetheless captures the experimental trend extremely well, especially when taken in direct comparison to figure 3, which modeled the result as an either/or situation: either noneroding or fully eroding penetration. The presence of the impact-pressure differential, ΔP , has permitted a better match to the residual velocities in figure 9b, for high striking velocities where the event is largely erosive. The methodology of rod-deformation-as-trigger for the erosion transition, embodied in the parameter ΔL_{CRIT} , has the primary bearing upon the residual length behavior modeled in figure 9a.

To ascertain whether the rod-deformation-as-trigger methodology adversely affects the previously considered Semi-Infinite Series test result that was so well captured in the preceding report (1) (shown in figure 1), the revised model is applied to that test series. Because the Al in both the Finite-Target Series and the Semi-Infinite Series I of tests are of the same hardness, the identical properties are retained for ΔL_{CRIT} ; namely, equal to $1.4D_0$. The result is shown in figure 10. While the residual velocity and penetration curves are slightly affected, the important aspect to note is that, for deep penetration, the erosion transition has an appearance of being an abrupt function of striking velocity, even though the results presented, for all impact velocities,

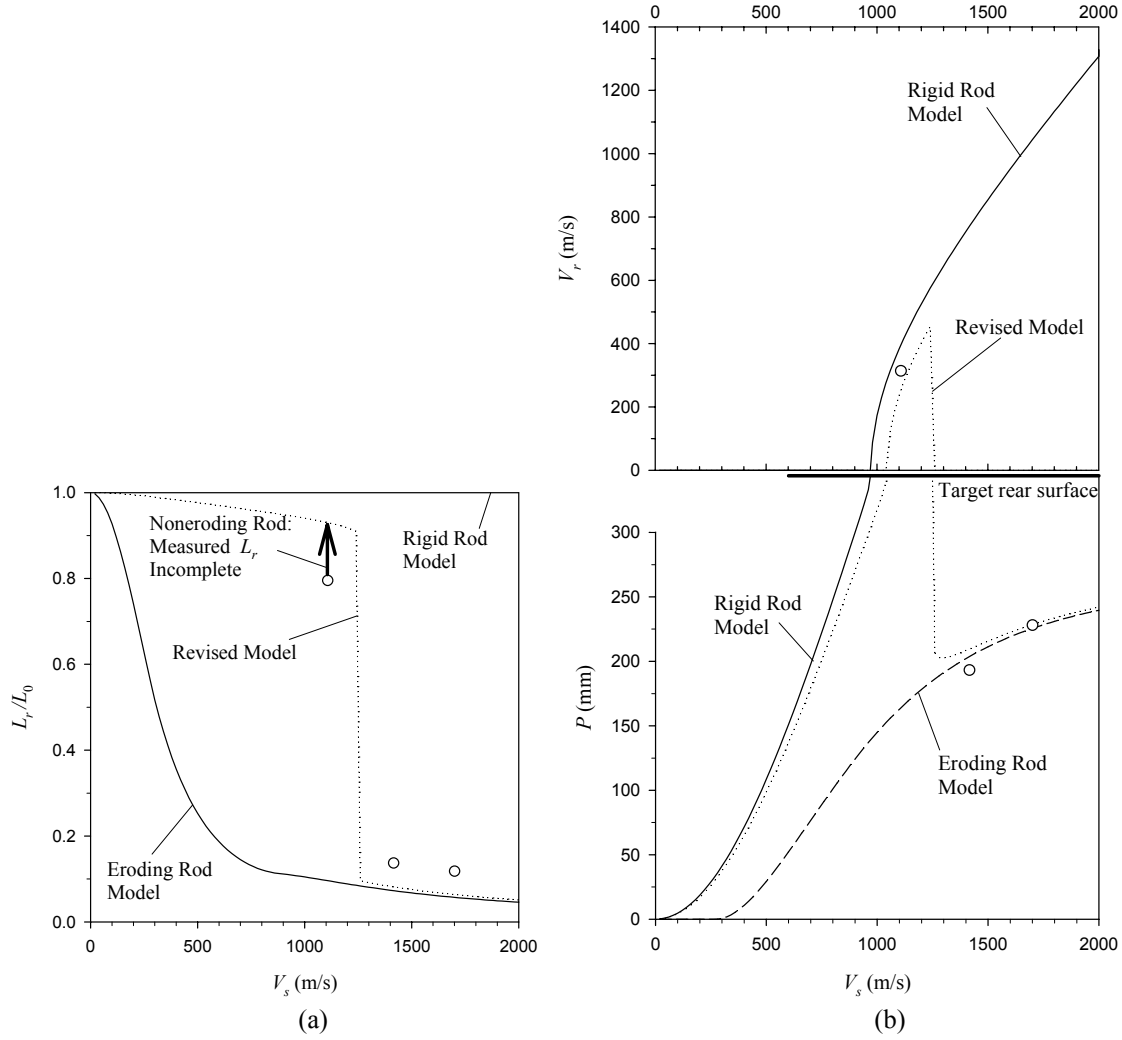


Figure 10. Data for Semi-Infinite Series I tests, with comparison to rigid-rod, eroding-rod, and revised-methodology calculations, for (a) residual rod length and (b) penetration and residual velocity.

undergo a noneroding phase at the onset of penetration. The transition point agrees with the current data set, falling between 1100 and 1400 m/s of striking velocity. The actual transition value, ~ 1200 m/s, also agrees well with the experimental observations reported by Scheffler (14) for WA rods striking Al-5083 targets.

Like the Finite-Target Series, the results of modeling the Interply Series data as either a purely rigid or purely eroding phenomenon did not match well with the experimental record, both for residual rod length (figure 5a) and residual velocity (figure 5b). The two varieties of Al target plies in the Interply Series of tests are substantially stronger than those in the Finite-Target Series and Semi-Infinite Series I tests. Based on the experimental record reported by Scheffler (14), who reported different erosion-transition velocities in two different Al alloys, it was anticipated that the propensity to sustain noneroding penetration, as captured by the ΔL_{CRIT} parameter, would

vary with target resistance. With no quantitative guidance on its selection, this parameter was fitted to obtain the best results for the Interply Series. The one self-imposed constraint enforced, for simplicity, was to keep ΔL_{CRIT} linear with target resistance, over the range of resistance from $H = 1.78$ – 2.77 GPa. This range of target resistances covers all data for the Semi-Infinite-Series I, the Finite-Target Series, and the Interply Series tests. Within this constraint, the selected values of ΔL_{CRIT} were $1.4D_0$ for $H = 1.78$ GPa, $1.65D_0$ for $H = 2.07$ GPa, and $2.25 D_0$ for $H = 2.77$ GPa, all of which are collinear in the plane of ΔL_{CRIT} vs. H .

With these values for the erosion-transition parameter ΔL_{CRIT} , the results of the revised model for the Interply Series are given in figure 11. Despite the scatter in the test data, the results appear to be a vast improvement over figure 5, again supporting the contention that an allowable rod deformation, as captured by ΔL_{CRIT} , is the relevant trigger for the onset of rod erosion.

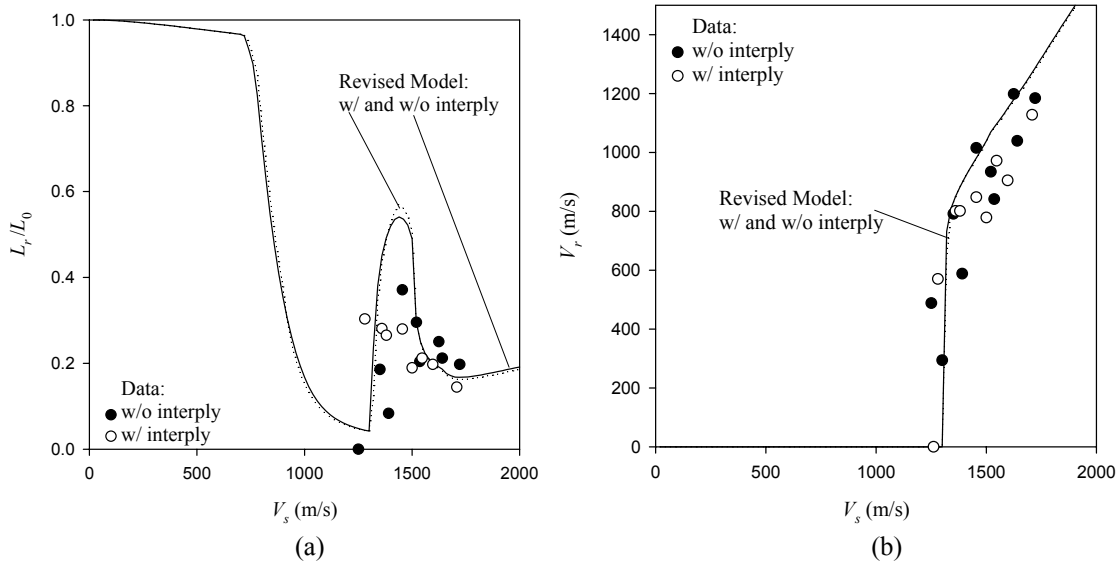


Figure 11. Data for Interply Series tests, with comparison to revised-methodology calculation, for (a) residual rod length and (b) residual velocity.

There was a single datum categorized as Semi-Infinite Series II, which involved the same rod impacting a much stronger BHN 190 target at 1413 m/s. The test result proves to be above the erosion threshold, having penetrated a mere 130.4 mm. However, this result is important, as figure 12a reveals that the parameter ΔL_{CRIT} cannot exceed a value of $1.2D_0$ while simultaneously predicting the ballistic result above the erosion threshold. For comparison, a result is plotted on the same graph that assumes ΔL_{CRIT} equal to $2.25D_0$ that shows the unlikelihood of this possibility. This datum shows the anticipated trend reversal in behavior of ΔL_{CRIT} with increasing H . As H increases, common sense dictates that ΔL_{CRIT} must eventually return to zero, and the datum here indicates that that trend reversal has already begun by the time H reaches 3.16 GPa.

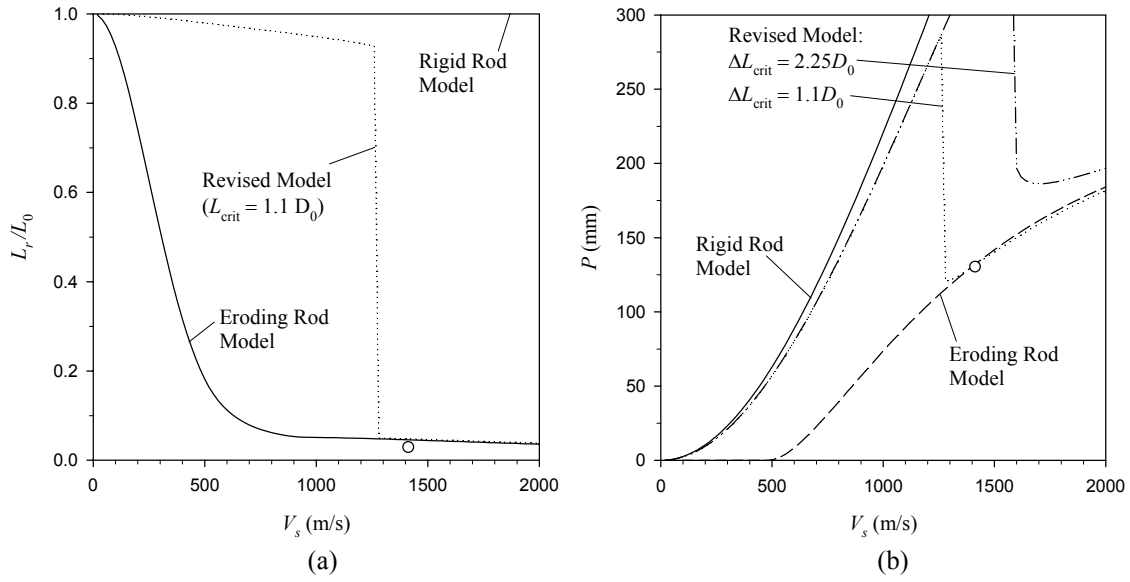


Figure 12. Datum for Semi-Infinite Series II test, with comparison to rigid-rod, eroding-rod, and revised-methodology calculations, for (a) residual rod length and (b) penetration (note: revised-methodology calculation shown for two values of parameter ΔL_{CRIT}).

A plot of the value of ΔL_{CRIT} with increasing H is shown in figure 13. Recall that these values for ΔL_{CRIT} are empirical, but are nonetheless buttressed by various experimental data. For example, Forrestal and Piekutowski (24) witnessed a length foreshortening of $1.43 D_0$ just below the erosion threshold for a configuration very comparable to the BHN 97 configuration in which $\Delta L_{CRIT} = 1.4 D_0$ is currently employed. And while the Semi-Infinite Series II datum cannot indicate precisely the value of ΔL_{CRIT} , it nonetheless serves to place an upper bound on its value for that rod/target configuration.

Modeling ΔL_{CRIT} as a function of H alone was permitted here only because of the invariant rod material and rod-nose shape across all the test series, as well as the limited impact-velocity span over which the tests were conducted. Unlike hemispherical-nosed (and conical- and ogive-nosed) rods, flat-nosed rods will have no kinematic tendency for an applied pressure at the contact surface to resist the penetrator's radial flow that brings about erosion. For this reason, one would expect flat-nosed rods to have severely retarded, if not absent, values of ΔL_{CRIT} . Similarly, while conical-nosed rods have a geometry that serves to restrain rod-nose material from flowing radially outward, their sudden transition in slope between the rod's nose and shank promotes, during penetration, a separation of target material from the rod at that point. Preventing this flow separation is essential to inhibiting the onset of erosion because a target not in contact with the rod can offer no lateral resistance to the emerging radial rod flow that is a precursor to erosion. It is thus no surprise that the phenomenology of erosion transition for conical-nose rods occurs not at the rod tip, but where the tip meets at the shank, as noted by Brooks and Erikson (10) and Woodward (12, 13).

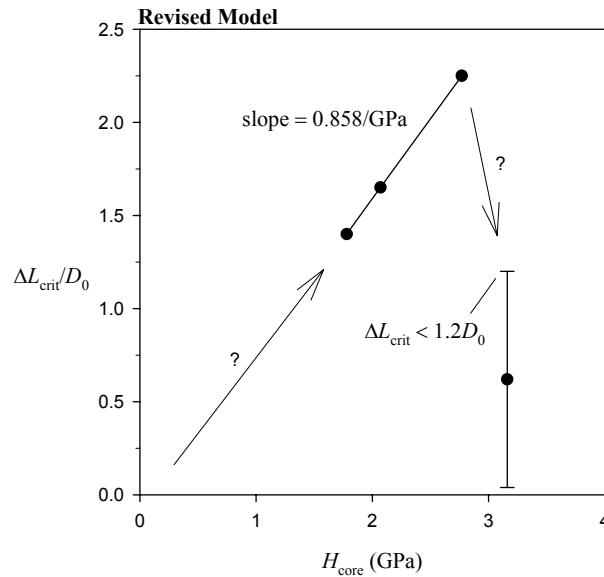


Figure 13. Rod-deformation-to-erosion-onset model parameter, $\Delta L_{\text{CRIT}}/D_0$, shown as a function of target resistance, for the Al alloys modeled in the current test series, with anticipated interpolation and extrapolation to other Al alloys.

Exploring the model's behavior has revealed several parameter sensitivities in general. The magnitude of H_{LAT} will primarily control the striking velocity at which significant deformation occurs. The impact-pressure transient ΔP only affects the residual velocity to any extent, and not the residual rod length. In semi-infinite penetration, the addition of a transient ΔP may depress the depth of penetration very slightly. The allowable rod deformation (i.e., length foreshortening parameter, ΔL_{CRIT}) that precedes the onset of erosion will primarily control the rapidity of the transition from a noneroding to a largely eroding event, and is therefore a significant factor in the residual length calculation.

5. Comparison to FZ Model

Comparison with the current model and experimental data is now offered against the FZ model (2, 3), on which the current model's development was originally based. Note, however, that the FZ model has not been updated to reflect the current thinking on the transition-velocity regime phenomenology. Rather, the comparison is performed against the existing FZ model using the preexisting modeling options to address this very issue of threshold-velocity penetration mechanics.

According to Frank (32), the FZ model is capable of modeling the dislocation in penetration associated with the erosion transition by utilizing a feature of the model, wherein the surface resistance of the target is set lower than the core resistance. The rationale for this approach is the indentation literature that shows the resistance to shallow indentation at a level roughly 1/3 that for deep indentation. Coupling this feature with the intrinsic FZ model behavior that precludes transition from rigid penetration to eroding penetration within a target element allows the model to penetrate rigidly throughout an event if the surface resistance can be set low enough to trigger an initially rigid response. Note that the approach of lowering the target resistance by the FZ model is the opposite of that proposed in the current model, in which the effective rod strength is raised by the presence of lateral confinement from the target. Nonetheless, both approaches have the effect of instigating noneroding penetration for rod/target combinations that would normally not experience it.

Allowing for the differences in modeling the rod's plastic zone cited in subsection 3.4.2, entitled "Extended Bernoulli Equation," the present comparison allows for the target resistances used in the FZ model to be elevated over their counterparts in the current model. The elevated values of H chosen in the FZ model were selected to produce comparable results for the purely eroding and purely rigid configurations. So, for example, where the BHN 97 Al is characterized with a target resistance of 1.78 GPa in the current model, a value of 2.10 GPa is employed in the FZ model. Other Al alloys in the FZ model are treated as follows: the BHN 112 alloy utilizes $H = 2.25$ GPa, the BHN 143 alloy utilizes $H = 2.95$ GPa, and the BHN 190 alloy utilizes $H = 3.55$ GPa. The results for the test series, employing purely rigid or purely penetration conditions, are given in figures 14–17.

From figure 15, it is observed that, for the purely eroding configuration, the influence of the thin steel backing is overly accentuated, compared with the current model in figure 3. For example, the FZ model is seen to predict an excessive 100 m/s difference in limit velocity from the addition of the thin target backplate. In the Interply Series results of figure 16, the effect is more pronounced, with the FZ model predicting the limit velocity to decrease by 150 m/s, with the addition of a thin acrylic element in the middle of the target. The nature of these deficiencies has been noted in the past (4, 5) and arises from the fact that the FZ penetration methodology only "looks ahead" one target element at a time to anticipate changes in target resistance. But other than these noted differences, the FZ model behaves, in most ways, similarly to the revised model for both eroding and purely rigid conditions of penetration.

Noting these differences between FZ and the current model for the purely eroding configurations, consider now the more complex problem of noneroding penetration and erosion transition. While technical arguments might justify a surface resistance at one third the core resistance, such a level in the FZ model produces a noneroding threshold into BHN 97 Al at ~550 m/s. Recall that the data show noneroding penetration at striking velocities beyond 1100 m/s. Stretching the justification beyond a prudent level to accentuate the effect, the surface resistance will be set as low as possible (zero, to be precise) to give the FZ model its best hope of

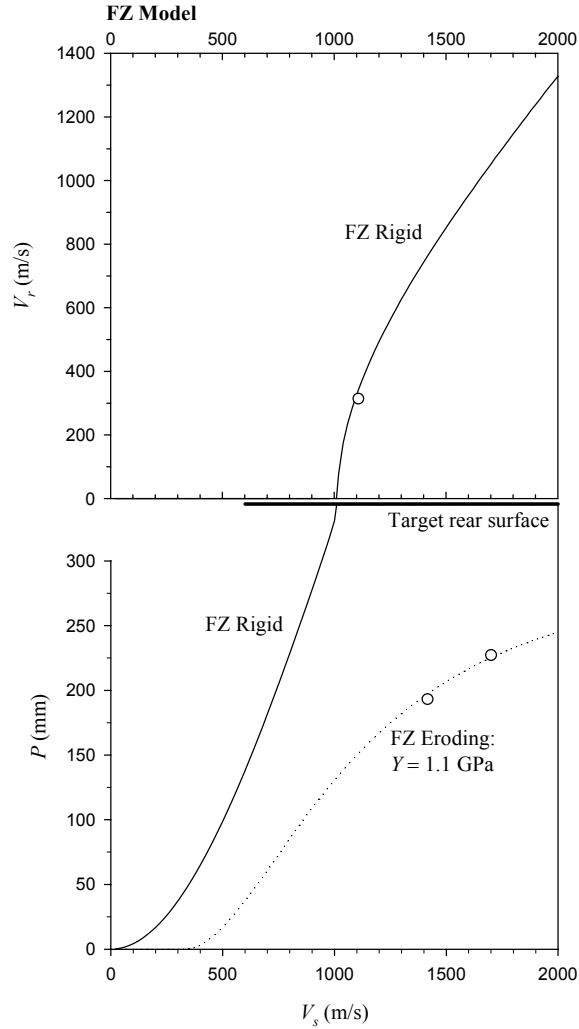


Figure 14. Penetration and residual-velocity data for Semi-Infinite Series I tests, with comparison to FZ-model results, for rigid and eroding rods.

matching the data. Even then, the threshold transition occurs at 900 m/s, as shown in figure 18, significantly below the empirically observed levels. In this figure, the nomenclature “-S” is used to denote the FZ model with the soft-surface feature employed. Other than the actual velocity of the eroding transition, figure 18 appears at first glance consistent with the phenomenology of how the eroding transition occurs in deep penetration events.

When attention is turned to the other test series, however, the FZ soft-surface methodology fares even more poorly. Figures 19 and 20 provide the results of the FZ methodology for the Finite-Target and Interply Series tests.

The influence of the soft-surface features of the FZ model are primarily limited to the lower striking velocities, and do not greatly influence the results at higher striking velocities from the

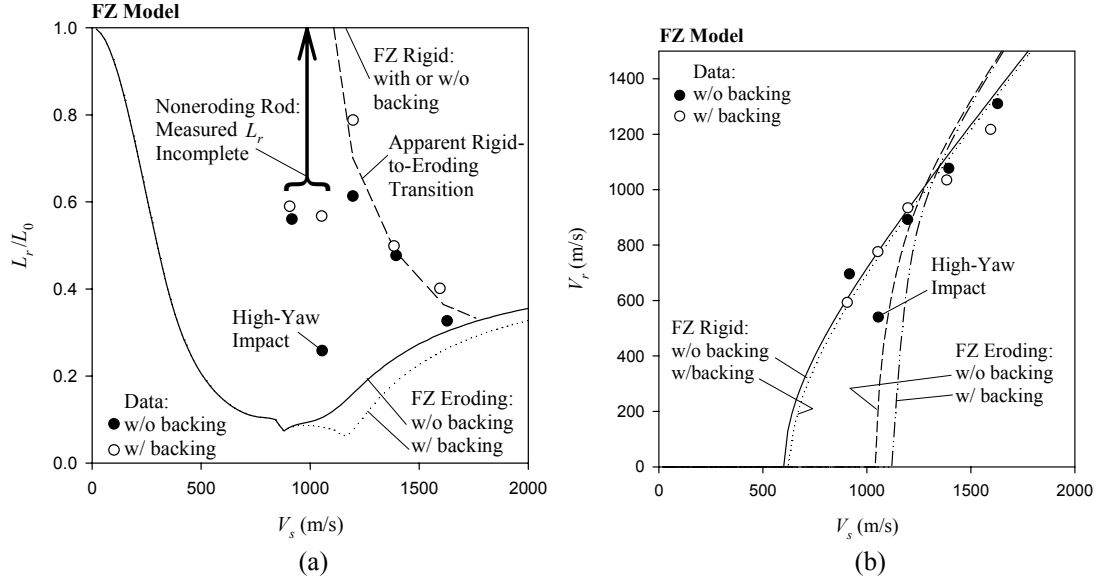


Figure 15. Data for Finite-Target Series tests, with comparison to FZ-rigid-model and FZ-eroding-model calculations, for (a) residual rod length and (b) residual velocity.

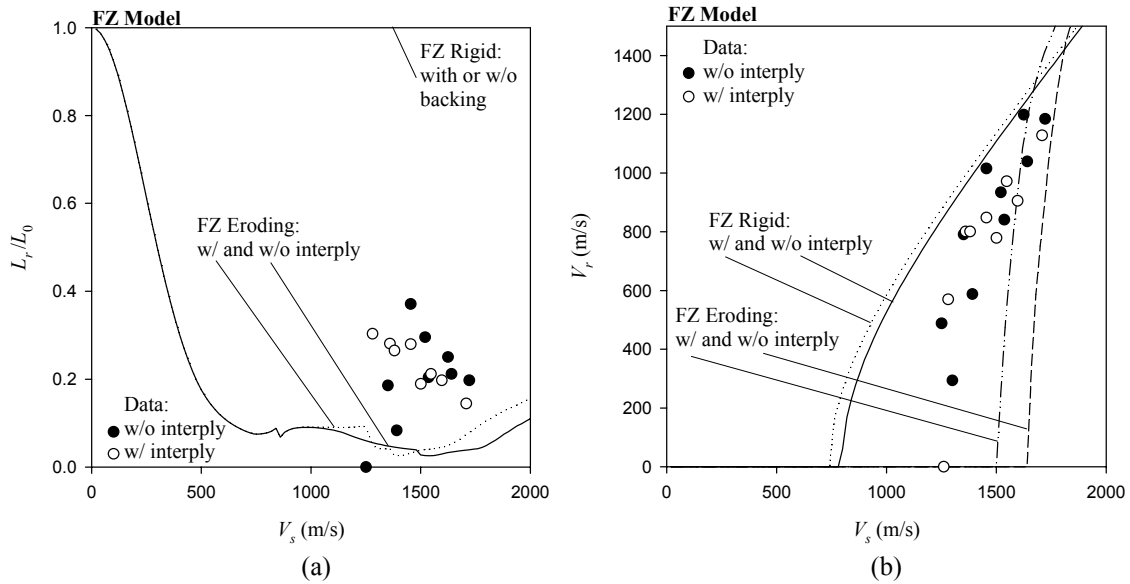


Figure 16. Data for Interply Series tests, with comparison to FZ-rigid-model and FZ-eroding-model calculations, for (a) residual rod length and (b) residual velocity.

basic eroding-only model. Additionally, the exaggerated effect on the FZ model predictions from the addition of ballistically negligible target elements is noted for both the Finite Target Series and Interply Series tests.

A comparison of the respective model's through-target treatment of effective rod strength and target resistance is provided in figure 21, for the Finite Target Series simulation at a striking velocity of 1250 m/s. The FZ model utilizes the soft-surface feature for target resistance

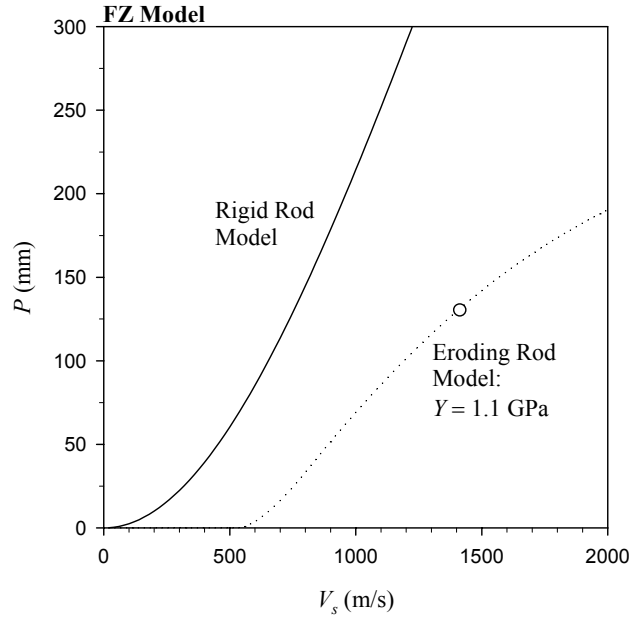


Figure 17. Penetration datum for Semi-Infinite Series II test, with comparison to FZ-model results, for rigid and eroding rods.

(figure 21a), whereas the revised model employs a lateral stress (H_{LAT}) augmentation to the axial stress state in the rod (figure 21b). In the revised model, when the axial rod stress (s_{AXIAL}) is at the maximum allowable level of $Y + H_{LAT}$, the rod generally will be penetrating in a deforming, yet noneroding, fashion.

The author considered the possibility that the preferred FZ implementation of soft-target surfaces was one that was intended not just at the leading surface of the target, but also at subsequent interfaces inside the target. But while such an interpretation did, in some cases, improve the overall appearance of the residual-length or residual-velocity results arising from the FZ model, it would require one to accept strength and resistance variations such as those presented in figure 22. In this figure, which reports the FZ model's strength characterization of the Finite Target Series simulation at a striking velocity of 1000 m/s, the nomenclature “-S/I” is used to denote the FZ model with the soft-surface and soft-interfaces feature employed. Note that figure 22 employs the soft interface only at the material boundary between the two different Al alloys, and not at every physical plate boundary in the target. Even so, the purported strength variation, as presented, strains the bounds of credulity and so attempts to improve results by employing such an interpretation were subsequently discarded.

The results of modeling the target with a soft surface, for a simple case like that presented in figure 18, may give the cursory impression of capturing the penetration dislocation associated with the erosion transition of the penetrator. However, a deeper investigation into a wider range of targets and engagement configurations reveals the inability of the preexisting FZ-modeling framework to capture the more general phenomenon.

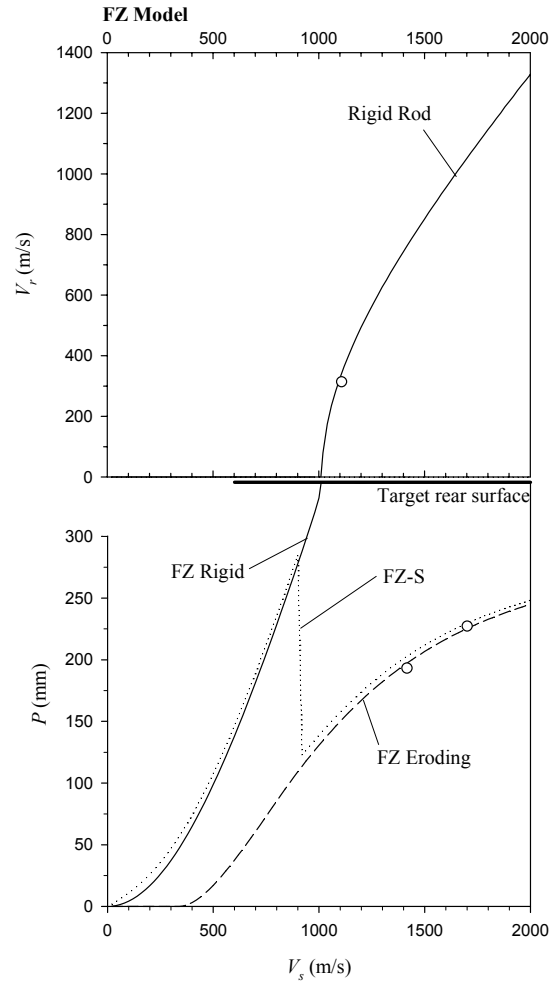


Figure 18. Penetration and residual-velocity data for Semi-Infinite Series I tests, with comparison to FZ-model results, for rigid and eroding rods and FZ-S model with soft target surface.

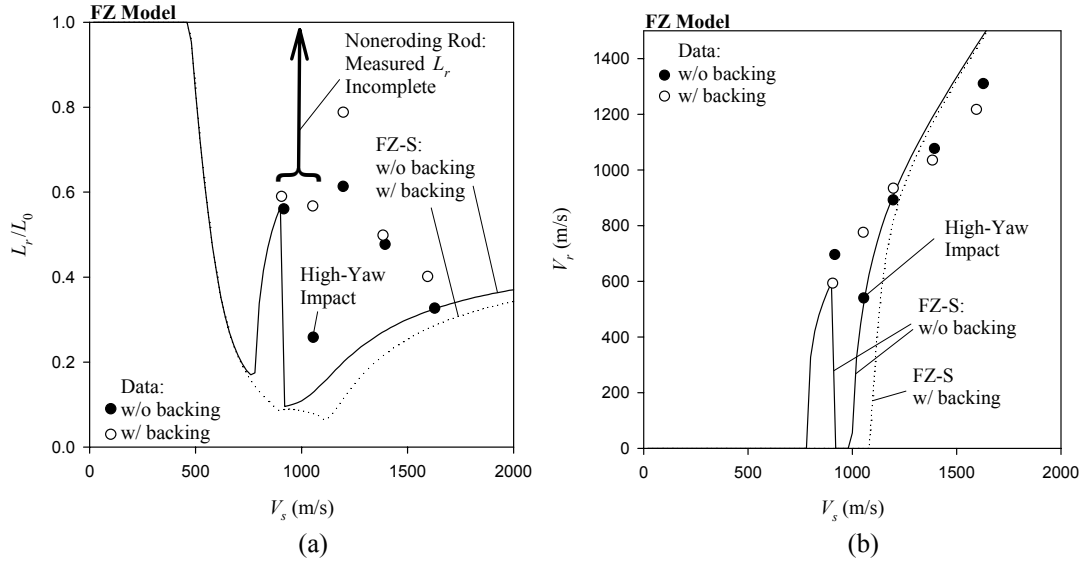


Figure 19. Data for Finite Target Series tests, with comparison to FZ-S (soft surface) model calculations, for (a) residual rod length and (b) residual velocity.

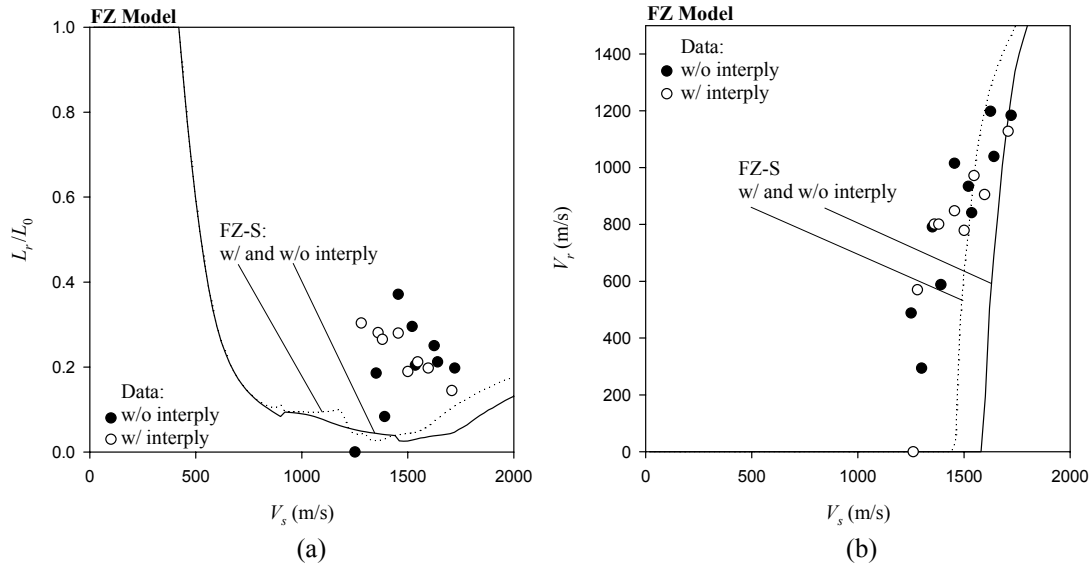


Figure 20. Data for Interply Series tests, with comparison to FZ-S (soft surface) model calculations, for (a) residual rod length and (b) residual velocity.

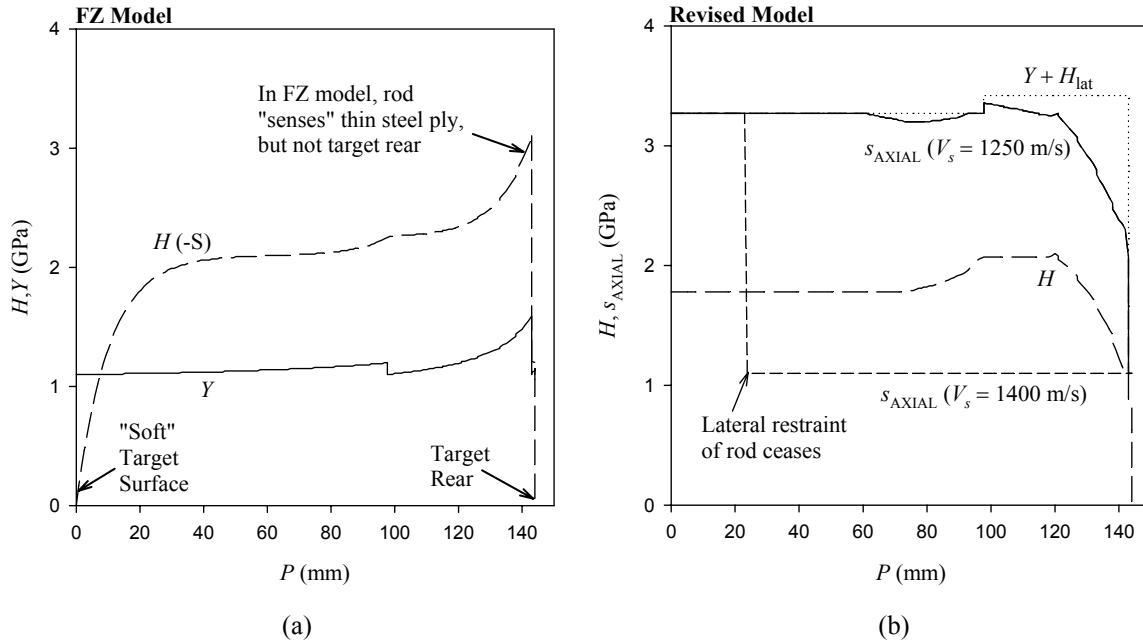


Figure 21. Target resistance and axial rod stress, through the depth of the Finite Target Series target at 1250 m/s striking velocity, as characterized by (a) the FZ-S (soft surface) model and (b) the revised model.

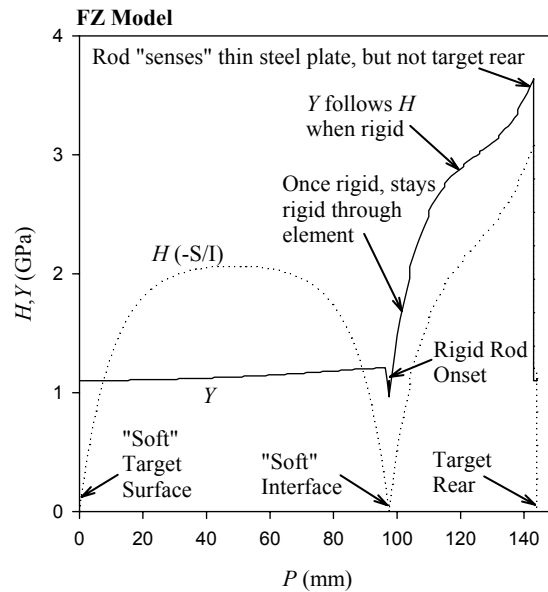


Figure 22. Target resistance and axial rod stress, through the depth of the Finite Target Series target at 1000 m/s striking velocity, as characterized by the FZ-S/I (soft surface and interfaces) model.

6. Conclusions

This report analyzes data related to the phenomenon of deforming, yet noneroding, penetration and the subsequent erosion transition of hemispherical-nosed WA $L/D = 15$ rods into laminate targets employing various alloys of Al and other materials. While the study of rigid-body penetration is well founded, a focus on long-rod penetration in which the penetrator experiences significant noneroding deformation has received more limited attention. More vaguely understood, still, are the conditions under which noneroding deformation transitions to fully eroding penetration.

The current report documents series of 34 experiments that probe the nature of this phenomenon under a variety of target configurations, from thick, monolithic Al to finite laminates composed of several materials. The tests were conducted over a striking-velocity range from 906 to 1722 m/s. Physical and radiographic data were collected, against which to compare any modeling, and include penetration, as well as residual length and residual velocity of the penetrator. Additionally, crater profiles were available for examination and occasional residual penetrator fragments were recovered. A model was formulated and tested against the data in an attempt to capture this wide range of data collected.

Aside from the traditional treatments of fully eroding or rigid-body penetration, the model has several key phenomenological elements that have been found necessary to address the issues at hand. They include the following:

- The presence, during the noneroding phase of penetration, of lateral confinement on the rod by the target wall, applying a lateral resistance $\sim 1.2 \times$ the target element's ballistic (axial) resistance;
- An augmentation, during the noneroding phase of penetration, of the rod's axial stress, in accordance with Tresca plasticity, and resulting from the lateral confinement of the rod;
- A trigger for erosion that is governed by a level of noneroding rod deformation associated with the target element's resistance (rod properties and especially rod-nose geometry will also affect the erosion trigger, but these are kept essentially invariant throughout the test series); and
- An accounting of the large transient impact pressure, insofar as its influence on rod deceleration.

In addition to these elements of model phenomenology, the solution methodology employs variations from the traditional method. In particular, for the noneroding phase of penetration, the rod deceleration equation is solved using a control volume that includes the complete rod, not just the elastic portion. Further, the rod's plastic zone size, during this noneroding phase, is

assumed to follow a generic functional form selected to minimize the net influence on the rod/target stress balance. These changes in solution methodology alleviate the need to quantify the difficult-to-know size of the plastic zone during the noneroding phase of penetration.

With this revised methodology, the experimental results for residual velocity and rod length have been nicely captured, for a variety of target configurations and over a range of impact velocities. Without the revised methodology, or using alternate methodologies (e.g., velocity-dependent erosion trigger and/or lateral resistance) that were explored, the match to data was drastically different and unacceptably poor. Further, attempts to employ the preexisting FZ methodology to the problem of noneroding penetration and erosion transition proved largely unsuccessful. The phenomenology proposed by the FZ model for noneroding penetration was one based upon the surface of a target having a lower resistance than the target's core. The implementation of the FZ methodology has the net effect of making the erosion transition a striking-velocity-dependent phenomenon, which was found to be a poor trigger for erosion onset.

One is led to the conclusion that a phenomenology like the one proposed, or very close to it, prevails during the special circumstances when deforming, yet noneroding, penetration occurs, leading up to the point where the transition to a traditional eroding event ensues. Perhaps the phenomenon is limited to the penetration of ductile low-density target materials, in which the crater radius is naturally small due to the high-penetration efficiencies. Nonetheless, unexplored areas warranting further study would include the influence of rod-nose geometry, rod material properties, and target materials other than Al.

7. References

1. Segletes, S. *Analysis of the Noneroding Penetration of Tungsten Alloy Long Rods Into Aluminum Targets*; ARL-TR-3075; U.S. Army Research Laboratory: Aberdeen Proving Ground, MD, 2003.
2. Zook, J. A.; Frank, K.; Silsby, G. F. *Terminal Ballistics Test and Analysis Guidelines for the Penetration Mechanics Branch*; BRL-MR-3960; U.S. Army Ballistic Research Laboratory: Aberdeen Proving Ground, MD, 1992.
3. Wright, T. W.; Frank, K. *Approaches to Penetration Problems*; BRL-TR-2957; U.S. Army Ballistic Research Laboratory: Aberdeen Proving Ground, MD, 1988.
4. Segletes, S. B. *An Adaptation of Walker-Anderson Model Elements Into the Frank-Zook Penetration Model for Use in MUVES*; ARL-TR-2336; U.S. Army Research Laboratory: Aberdeen Proving Ground, MD, 2000.
5. Segletes, S. B.; Grote, R.; Polesne, J. *Improving the Rod-Penetration Algorithm for Tomorrow's Armors*; ARL-RP-23; U.S. Army Research Laboratory: Aberdeen Proving Ground, MD, 2001.
6. Walker, J. D.; Anderson, C. E., Jr. A Time-Dependent Model for Long-Rod Penetration. *International Journal of Impact Engineering* **1995**, *16* (1), 19–48.
7. Tate, A. A Theory for the Deceleration of Long Rods After Impact. *Journal of Mechanics and Physics of Solids* **1967**, *15*, 387–399.
8. Alekseevskii, V. Penetration of a Rod Into a Target at High Velocity. *Combustion, Explosions, and Shock Waves* **1966**, *2*, 63–66.
9. Kinslow, R. Collisions at High Velocity. *International Science and Technology* **1965**, *40*.
10. Brooks, P. N.; Erikson, W. H. *Ballistic Evaluation of Materials for Armour Penetrators*; DREV R-643/71; Defence Research Establishment Valcartier: Quebec, Canada, 1971.
11. Hill, R. Cavitation and the Influence of Headshape in Attack of Thick Targets by Non-Deforming Projectiles. *Journal of Mechanics and Physics of Solids* **1980**, *28*, 249–263.
12. Woodward, R. L. A Note on the Deformation of Conical Penetrators. *International Journal of Impact Engineering* **1984**, *2* (4), 325–330.
13. Woodward, R. L. The Effect of Projectile Tip Geometry on Penetration Into Semi-Infinite Metal Targets. *Proceedings of the 9th International Symposium on Ballistics*, Shrivenham, U.K., May 1986.

14. Scheffler, D. R. *Modeling the Effect of Penetrator Nose Shape on Threshold Velocity for Thick Aluminum Targets*; ARL-TR-1417; U.S. Army Research Laboratory: Aberdeen Proving Ground, MD, 1997.
15. Scheffler, D. R. *Modeling Threshold Velocity of Hemispherical and Ogival-Nose Tungsten-Alloy Penetrators Perforating Finite Aluminum Targets*; ARL-TR-1583; U.S. Army Research Laboratory: Aberdeen Proving Ground, MD, 1998.
16. Magness, L. S.; Scheffler, D. R. The Influence of Penetrator Material and Projectile Nose Shape on the Onset of Penetrator Deformation and Erosion. *Proceedings of the 2nd Australasian Conference on Applied Mechanics*, Canberra, Australia, February 1999.
17. Yatteau, J. D.; Dzwilewski, P. T. The Onset of Deformation and Flow in Penetrators With Conical Noses. *Proceedings of the 15th International Symposium on Ballistics*, Jerusalem, Israel, 21–24 May 1995.
18. Warren, T. L. Simulations of the Penetration of Limestone Targets by Ogive-Nosed 4340 Steel Projectiles. *International Journal of Impact Engineering* **2002**, *27*, 475–496.
19. Forrestal, M. J.; Okajima, K.; Luk, V. K. Penetration of 6061-T651 Aluminum Targets With Rigid Long Rods. *Journal of Applied Mechanics* **1988**, *55*, 755–760.
20. Rosenberg, A.; Forrestal, M. J. Perforation of Aluminum Plates With Conical-Nosed Rods – Additional Data and Discussion. *Transactions of the ASME* **1988**, *55*, 236–238.
21. Forrestal, M.; Luk, V. K. Perforation of Aluminum Armor Plates With Rigid Conical-Nose Projectiles. *Mechanics of Materials* **1990**, *10*, 97–105.
22. Forrestal, M.; Brar, N. S.; Luk, V. K. Penetration of Strain-Hardening Targets With Rigid Spherical-Nose Rods. *Journal of Applied Mechanics* **1991**, *58*, 7–10.
23. Forrestal, M.; Luk, V. K.; Rosenberg, Z.; Brar, N. S. Penetration of 7075-T651 Aluminum Targets With Ogival-Nose Rods. *International Journal of Solids and Structures* **1992**, *29* (14/15), 1729–1736.
24. Forrestal, M. J.; Piekutowski, A. J. Penetration Experiments With 6061-T6511 Aluminum Targets and Spherical-Nose Steel Projectiles at Striking Velocities Between 0.5 and 3.0 km/s. *International Journal of Impact Engineering* **2000**, *24*, 51–67.
25. Piekutowski, A. J.; Forrestal, M. J.; Poorman, K. L.; Warren, T. L. Penetration of 6061-T6511 Aluminum Targets by Ogive-Nose Steel Projectiles With Striking Velocities Between 0.5 and 3.0 km/s. *International Journal of Impact Engineering* **1999**, *23*, 723–734.
26. Wijk, A. G. High-Velocity Projectile Penetration Into Thick Armour Targets. *International Journal of Impact Engineering* **1999**, *22*, 45–54.

27. Segletes, S. B.; Walters, W. P. A Note on the Application of the Extended Bernoulli Equation. *International Journal of Impact Engineering* **2002**, 27, 561–576.
28. Tabor, D. *The Hardness of Metals*, Chapter IV; Oxford University Press: New York, 1951.
29. Hopkins, H. G. Dynamic Expansion of Spherical Cavities in Metals. *Progress in Solid Mechanics* **1960**, 1 (3), Sneddon, I. N., Hill, R., Eds.; North Holland Publishing: Amsterdam.
30. Goodier, J. N. On the Mechanics of Indentation and Cratering in Solid Targets of Strain-Hardening Metal by Impact of Hard and Soft Spheres. *Proceedings of the 7th Hyper-Velocity Impact Symposium, Volume III—Theory*, Orlando, FL, **1965**, 215–259.
31. Hanagud, S.; Ross, B. Large Deformation, Deep Penetration Theory for a Compressible Strain-Hardening Target Material. *AIAA Journal* **1971**, 9 (5).
32. Frank, K. U.S. Army Research Laboratory, Aberdeen Proving Ground, MD. Private communication, February 2003.

NO. OF
COPIES ORGANIZATION

1
(PDF
Only) DEFENSE TECHNICAL
INFORMATION CENTER
DTIC OCA
8725 JOHN J KINGMAN RD
STE 0944
FT BELVOIR VA 22060-6218

1 COMMANDING GENERAL
US ARMY MATERIEL CMD
AMCRDA TF
5001 EISENHOWER AVE
ALEXANDRIA VA 22333-0001

1 INST FOR ADVNCD TCHNLGY
THE UNIV OF TEXAS
AT AUSTIN
3925 W BRAKER LN STE 400
AUSTIN TX 78759-5316

1 US MILITARY ACADEMY
MATH SCI CTR EXCELLENCE
MADN MATH
THAYER HALL
WEST POINT NY 10996-1786

1 DIRECTOR
US ARMY RESEARCH LAB
AMSRD ARL D
DR D SMITH
2800 POWDER MILL RD
ADELPHI MD 20783-1197

1 DIRECTOR
US ARMY RESEARCH LAB
AMSRD ARL CS IS R
2800 POWDER MILL RD
ADELPHI MD 20783-1197

3 DIRECTOR
US ARMY RESEARCH LAB
AMSRD ARL CI OK TL
2800 POWDER MILL RD
ADELPHI MD 20783-1197

3 DIRECTOR
US ARMY RESEARCH LAB
AMSRD ARL CS IS T
2800 POWDER MILL RD
ADELPHI MD 20783-1197

NO. OF
COPIES ORGANIZATION

ABERDEEN PROVING GROUND

1 DIR USARL
AMSRD ARL CI OK TP (BLDG 4600)

<u>NO. OF COPIES</u>	<u>ORGANIZATION</u>	<u>NO. OF COPIES</u>	<u>ORGANIZATION</u>
4	DEFENSE THREAT REDUCTION AGY J LYON K W HUNTER T FREDERICKSON R J LAWRENCE 8725 JOHN J KINGMAN RD STOP 6201 FT BELVOIR VA 22060-6201	3	COMMANDER US ARMY RESEARCH OFFICE K IYER J BAILEY S F DAVIS PO BOX 12211 RESEARCH TRIANGLE PARK NC 27709-2211
2	COMMANDER US ARMY ARDEC AMSTA AR FSA E W P DUNN E BAKER PICATINNY ARSENAL NJ 07806-5000	1	NAVAL AIR WARFARE CTR S A FINNEGAN BOX 1018 RIDGECREST CA 93556
1	COMMANDER US ARMY ARDEC AMSTA AR CCH V M D NICOLICH PICATINNY ARSENAL NJ 07806-5000	4	COMMANDER NAVAL WEAPONS CENTER N FASIG CODE 3261 T T YEE CODE 3263 D THOMPSON CODE 3268 W J MCCARTER CODE 6214 CHINA LAKE CA 93555
1	COMMANDER US ARMY ARDEC E ANDRICOPOULOS PICATINNY ARSENAL NJ 07806-5000	12	COMMANDER NAVAL SURFACE WARFARE CTR DAHLGREN DIVISION H CHEN D L DICKINSON CODE G24 C R ELLINGTON C R GARRETT CODE G22 W HOLT CODE G22 W E HOYE G22 R MCKEOWN J M NELSON M J SILL CODE H11 W J STROTHER A B WARDLAW JR L F WILLIAMS CODE G33 17320 DAHLGREN RD DAHLGREN VA 22448
1	COMMANDER USA STRATEGIC DEFNS CMD CSSD H LL T CROWLES HUNTSVILLE AL 35807-3801	2	AIR FORCE ARMAMENT LAB AFATL DLJR J FOSTER D LAMBERT EGLIN AFB FL 32542-6810
4	COMMANDER US ARMY AVIATION & MISSILE CMD AMSAM RD PS WF S HILL D LOVELACE M SCHEXNAYDER G SNYDER REDSTONE ARSENAL AL 35898-5247	1	USAF PHILLIPS LABORATORY VTSI R ROYBAL KIRTLAND AFB NM 87117-7345
1	COMMANDER US ARMY AVIATION & MISSILE CMD AMSAM RD SS AA J BILLINGSLEY REDSTONE ARSENAL AL 35898		
1	MIS DEFNS & SPACE TECHNOLOGY CSSD SD T K H JORDAN PO BOX 1500 HUNTSVILLE AL 34807-3801		

NO. OF
COPIES ORGANIZATION

2 USAF PHILLIPS LABORATORY
PL WSCD F ALLAHDADI
PV VTA D SPENCER
3550 ABERDEEN AVE SE
KIRTLAND AFB NM 87117-5776

1 AFIT ENC
D A FULK
WRIGHT PATTERSON AFB OH 45433

1 FBI
FBI LAB EXPLOSIVES UNIT
M LEONE
935 PENNSYLVANIA AVE NW
WASHINGTON DC 20535

7 LOS ALAMOS NATL LAB
L HULL MS A133
J V REPA MS A133
J WALTER MS C305
C WINGATE MS D413
E J CHAPYAK MS F664
P HOWE MS P915
J KENNEDY MS P915
PO BOX 1663
LOS ALAMOS NM 87545

3 DIRECTOR
LLNL
MS L35
D BAUM
M MURPHY
T MCABEE
PO BOX 808
LIVERMORE CA 94550

7 DIRECTOR
LLNL
MS L122
R PIERCE
R ROSINKY
O J ALFORD
D STEWART
T VIDLAK
B R BOWMAN
W DIXON
PO BOX 808
LIVERMORE CA 94550

NO. OF
COPIES ORGANIZATION

2 DIRECTOR
LLNL
MS L125
D R FAUX
N W KLINO
PO BOX 808
LIVERMORE CA 94550

31 SANDIA NATIONAL LABORATORIES
ATTN MAIL SERVICES MS 0100
J ANG MS 0310
P YARRINGTON MS 0310
W TEDESCHI MS 0479
B LEVIN MS 0706
A ROBINSON MS 0819
T TRUCANO MS 0819
P TAYLOR MS 0820
R BRANNON MS 0820
M KIPP MS 0820
D CRAWFORD MS 0820
L CHHABILDAS MS 0821
P STANTON MS 0821
J M MCGLAUN MS 0835
E S HERTEL JR MS 0836
L N KMETYK MS 0980
R REEDER MS 0980
J SOUTHWARD MS 0980
R LAFARGE MS 0986
R TACHAU MS 1156
M FURNISH MS 1168
M FORRESTAL MS 1174
W REINHART MS 1181
D HAYES MS 1181
J ASAY MS 1181
E W REECE MS 1185
D P KELLY MS 1185
C HALL MS 1209
J COREY MS 1217
C HILLS MS 1411
M VIGIL MS 1454
R O NELLUMS
PO BOX 5800
ALBUQUERQUE NM 87185-0100

1 DIRECTOR
LLNL
MS L149
R VAROSH
PO BOX 808
LIVERMORE CA 94550

<u>NO. OF COPIES</u>	<u>ORGANIZATION</u>
1	DIRECTOR LLNL R BARKER L159 PO BOX 808 LIVERMORE CA 94550
3	DIRECTOR LLNL MS L163 M FINGER R PERRET W SHOTTS PO BOX 808 LIVERMORE CA 94550
3	DIRECTOR LLNL MS L178 H KRUGER G POMYKAL M GERASSIMENKO PO BOX 808 LIVERMORE CA 94550
2	DIRECTOR LLNL MS L180 G SIMONSON A SPERO PO BOX 808 LIVERMORE CA 94550
1	DIRECTOR LLNL F A HANDLER L182 PO BOX 808 LIVERMORE CA 94550
1	DIRECTOR LLNL MS L282 W TAO PO BOX 808 LIVERMORE CA 94550
2	DIRECTOR LLNL MS L290 A HOLT J E REAUGH PO BOX 808 LIVERMORE CA 94550

<u>NO. OF COPIES</u>	<u>ORGANIZATION</u>
1	DIRECTOR LLNL S G COCHRAN L389 PO BOX 808 LIVERMORE CA 94550
2	DIRECTOR LLNL MS L495 D GAVEL J HUNTER PO BOX 808 LIVERMORE CA 94550
1	DIRECTOR LLNL R M KUKLO L874 PO BOX 808 LIVERMORE CA 94550
4	ENERGETIC MAT RSCH TSTG CTR NEW MEXICO TECH D J CHAVEZ L LIBERSKY F SANDSTROM M STANLEY CAMPUS STATION SOCORRO NM 87801
3	NASA JOHNSON SPACE CTR E CHRISTIANSEN J L CREWS F HORZ MAIL CODE SN3 2101 NASA RD 1 HOUSTON TX 77058
1	APPLIED RESEARCH LAB J A COOK 10000 BURNETT ROAD AUSTIN TX 78758
4	JET PROPULSION LABORATORY IMPACT PHYSICS GROUP Z SEKANINA P WEISSMAN B WEST J ZWISSLER 4800 OAK GROVE DR PASADENA CA 91109

<u>NO. OF COPIES</u>	<u>ORGANIZATION</u>	<u>NO. OF COPIES</u>	<u>ORGANIZATION</u>
2	BROWN UNIVERSITY R CLIFTON (ENGNG) P SCHULTZ (GEO SCI) PROVIDENCE RI 02912	1	NC STATE UNIVERSITY Y HORIE RALEIGH NC 27695-7908
2	CALTECH J SHEPHERD MS 105 50 A P INGERSOLL MS 170 25 1201 E CALIFORNIA BLVD PASADENA CA 91125	1	PA STATE UNIVERSITY PHYSICS DEPT UNIVERSITY PARK PA 16802
1	CALTECH G ORTON MS 169 237 4800 OAK GROVE DR PASADENA CA 91007	4	SOUTHWEST RESEARCH INSTITUTE C ANDERSON S A MULLIN J RIEGEL J WALKER PO DRAWER 28510 SAN ANTONIO TX 78228-0510
2	DREXEL UNIVERSITY MEM DEPT A ZAVALIANGOS (DEPT MAT ENGNG) 32ND & CHESTNUT ST PHILADELPHIA PA 19104	1	SUNY STONEYBROOK DEPT APPL MATH & STAT J GLIMM STONEYBROOK NY 11794
1	GEORGIA INSTITUTE OF TECH COMPUTATIONAL MODELING CTR S ATLURI ATLANTA GA 30332-0356	1	UC BERKELEY MECHANICAL ENGINEERING DEPT GRADUATE OFFICE K LI BERKELEY CA 94720
1	GEORGIA INSTITUTE OF TECH SCHOOL OF MATL SCI & ENGNG K LOGAN ATLANTA GA 30332-0245	2	UC SAN DIEGO DEPT APPL NECH & ENGR SVCS R011 S NEMAT NASSER M MEYERS LA JOLLA CA 92093-0411
1	JOHNS HOPKINS UNIVERSITY MAT SCI & ENGNG DEPT M LI 102 MARYLAND HALL 3400 N CHARLES ST BALTIMORE MD 21218-2689	2	UNIV OF ALA HUNTSVILLE AEROPHYSICS RSCH CTR G HOUGH D J LIQUORNIK PO BOX 999 HUNTSVILLE AL 35899
5	JOHNS HOPKINS UNIVERSITY APPLIED PHYSICS LAB T R BETZER A R EATON R H KEITH D K PACE R L WEST JOHNS HOPKINS ROAD LAUREL MD 20723	1	UNIV OF ALA HUNTSVILLE MECH ENGRNG DEPT W P SCHONBERG HUNTSVILLE AL 35899
1	LOUISIANA STATE UNIVERSITY R W COURTER 948 WYLIE DR BATON ROUGE LA 70808	2	UNIVERSITY DAYTON RSCH INST N BRAR A PIEKUTOWSKI 300 COLLEGE PARK DAYTON OH 45469-0182

<u>NO. OF COPIES</u>	<u>ORGANIZATION</u>	<u>NO. OF COPIES</u>	<u>ORGANIZATION</u>
3	UNIV DELAWARE DEPT OF MECH ENGN J GILLESPIE J VINSON D WILKINS NEWARK DE 19716	2	APPLIED RESEARCH ASSOC INC D GRADY F MAESTAS SUITE A220 4300 SAN MATEO BLVD NE ALBUQUERQUE NM 87110
1	UNIV ILLINOIS PHYSICS BUILDING A V GRANATO URBANA IL 61801	1	APPLIED RESEARCH LAB T M KIEHNE PO BOX 8029 AUSTIN TX 78713-8029
1	UNIV PENNSYLVANIA P A HEINEY DEPT OF PHYSICS & ASTRONOMY 209 SOUTH 33RD ST PHILADELPHIA PA 19104	1	ATA ASSOCIATES W ISBELL PO BOX 6570 SANTA BARBARA CA 93111
1	UNIV TEXAS DEPT OF MECH ENGINEERING E P FAHRENTHOLD AUSTIN TX 78712	1	BAE SYS ANALYTICAL SOLUTIONS M B RICHARDSON 1525 PERIMETER PKWY SUITE 500 HUNTSVILLE AL 35806
1	VA POLYTECHNIC INSTITUTE COLLEGE OF ENGINEERING DEPT ENGN SCI & MECHANICS R C BATRA BLACKSBURG VA 24061-0219	1	BRIGS CO J E BACKOFEN 2668 PETERSBOROUGH ST HERNDON VA 20171-2443
2	AEROJET J CARLEONE S KEY PO BOX 13222 SACRAMENTO CA 95813-6000	1	CENTURY DYNAMICS INC N BIRNBAUM 1001 GALAXY WAY SUITE 325 CONCORD CA 94583-1613
2	AEROJET ORDNANCE P WOLF G PADGETT 1100 BULLOCH BLVD SOCORRO NM 87801	1	COMPUTATIONAL MECHANICS CONSULTANTS J A ZUKAS PO BOX 11314 BALTIMORE MD 21239-0314
1	M L ALME 2180 LOMA LINDA DR LOS ALAMOS NM 87544-2769	1	CYPRESS INTERNATIONAL A CAPONECCHI 1201 E ABINGDON DR ALEXANDRIA VA 22314
1	APPLIED RESEARCH ASSOC INC J D YATTEAU SUITE 100 5941 S MIDDLEFIELD RD LITTLETON CO 80123	3	DOW CHEMICAL INC ORDNANCE SYSTEMS C HANEY A HART B RAFANIELLO 800 BUILDING MIDLAND MI 48667

<u>NO. OF COPIES</u>	<u>ORGANIZATION</u>
1	G E DUVALL 5814 NE 82ND CT VANCOUVER WA 98662-5944
3	DE TECHNOLOGIES INC P C CHOU R CICCARELLI W FLIS 3620 HORIZON DR KING OF PRUSSIA PA 19406
3	DYNASEN J CHAREST M CHAREST M LILLY 20 ARNOLD PL GOLETA CA 93117
1	R J EICHELBERGER 409 W CATHERINE ST BEL AIR MD 21014-3613
1	ELORET INSTITUTE NASA AMES RESEARCH CENTER D W BOGDANOFF MS 230 2 MOFFETT FIELD CA 94035
1	EXPLOSIVE TECHNOLOGY M L KNAEBEL PO BOX KK FAIRFIELD CA 94533
1	GB TECH LOCKHEED J LAUGHMAN 2200 SPACE PARK SUITE 400 HOUSTON TX 77258
2	GB TECH LOCKHEED L BORREGO C23C J FALCON JR C23C 2400 NASA ROAD 1 HOUSTON TX 77058
6	GDLS 38500 MOUND RD W BURKE MZ 436 21 24 G CAMPBELL MZ 436 30 44 D DEBUSSCHER MZ 436 20 29 J ERIDON MZ 436 21 24 W HERMAN MZ 435 01 24 S PENTESCU MZ 436 21 24 STERLING HTS MI 48310-3200

<u>NO. OF COPIES</u>	<u>ORGANIZATION</u>
1	GENERAL RESEARCH CORP T MENNA PO BOX 6770 SANTA BARBARA CA 93160-6770
1	RAYTHEON MSL SYS CO T STURGEON BLDG 805 M/S D4 PO BOX 11337 TUCSON AZ 85734-1337
5	INST FOR ADVANCED TECHNOLOGY S J BLESS J CAZAMIAS J DAVIS H D FAIR D LITTLEFIELD 3925 W BRAKER LN SUITE 400 AUSTIN TX 78759-5316
1	INTERNATIONAL RESEARCH ASSOC D L ORPHAL 4450 BLACK AVE PLEASANTON CA 94566
1	INTERPLAY F E WALKER 584 W TREELINE DR ALPINE UT 84004
1	ITT SCIENCES AND SYSTEMS J WILBECK 600 BLVD SOUTH SUITE 208 HUNTSVILLE AL 35802
1	R JAMESON 624 ROWE DR ABERDEEN MD 21001
1	KAMAN SCIENCES CORP D L JONES 2560 HUNTINGTON AVE SUITE 200 ALEXANDRIA VA 22303

<u>NO. OF COPIES</u>	<u>ORGANIZATION</u>	<u>NO. OF COPIES</u>	<u>ORGANIZATION</u>
7	KAMAN SCIENCES CORP J ELDER R P HENDERSON D A PYLES F R SAVAGE J A SUMMERS T W MOORE T YEM 600 BLVD S SUITE 208 HUNTSVILLE AL 35802	2	NETWORK COMPUTING SER INC T HOLMQUIST G JOHNSON 1200 WASHINGTON AVE S MINNEAPOLIS MN 55415
1	D R KENNEDY & ASSOC INC D KENNEDY PO BOX 4003 MOUNTAIN VIEW CA 94040	1	PHYSICAL SCIENCES INC P NEBOLSINE 20 NEW ENGLAND BUS CTR ANDOVER MA 01810
1	LOCKHEED MARTIN ELEC & MSLS G W BROOKS 5600 SAND LAKE RD MP 544 ORLANDO FL 32819-8907	2	GD OTS D BOEKA N OUYE 400 ESTUDILLO AVE SUITE 100 SAN LEANDRO CA 94577-0205
1	LOCKHEED MARTIN MISSILE & SPACE W R EBERLE PO BOX 070017 HUNTSVILLE AL 35807	1	PRC INC J ADAMS 5166 POTOMAC DR 103 KING GEORGE VA 22485-5824
3	LOCKHEED MARTIN MISSILE & SPACE M A LEVIN ORG 81 06 BLDG 598 M R MCHENRY T A NGO ORG 81 10 BLDG 157 111 LOCKHEED WAY SUNNYVALE CA 94088	1	RAYTHEON ELECTRONIC SYSTEMS R LLOYD 50 APPLE HILL DR TEWKSBURY MA 01876
4	LOCKHEED MISSILE & SPACE CO J R ANDERSON W C KNUDSON S KUSUMI 0 81 11 BLDG 157 J PHILLIPS 0 54 50 PO BOX 3504 SUNNYVALE CA 94088	1	ROCKWELL INTERNATIONAL ROCKETDYNE DIVISION H LEIFER 16557 PARK LN CIRCLE LOS ANGELES CA 90049
1	LOCKHEED MISSILE & SPACE CO R HOFFMAN SANTA CRUZ FACILITY EMPIRE GRADE RD SANTA CRUZ CA 95060	1	SAIC M W MCKAY 10260 CAMPUS POINT DR SAN DIEGO CA 92121
1	MCDONNELL DOUGLAS ASTRONAUTICS CO B L COOPER 5301 BOLSA AVE HUNTINGTON BEACH CA 92647	1	SHOCK TRANSIENTS INC D DAVISON BOX 5357 HOPKINS MN 55343
		2	SOUTHERN RESEARCH INSTITUTE L A DECKARD D P SEGERS PO BOX 55305 BIRMINGHAM AL 35255-5305
		1	ZERNOW TECHNICAL SVCS INC L ZERNOW 425 W BONITA AVE SUITE 208 SAN DIMAS CA 91773

NO. OF
COPIES ORGANIZATION

5 SRI INTERNATIONAL
J D COLTON
D CURRAN
R KLOOP
R L SEAMAN
D A SHOCKEY
333 RAVENSWOOD AVE
MENLO PARK CA 94025

ABERDEEN PROVING GROUND

62 DIR USARL
AMSRD ARL SL B
P TANENBAUM
AMSRD ARL SL BB
D DIETRICH
AMSRD ARL SL BD
R GROTE
J POLESNE
AMSRD ARL SL BE
D BELY
AMSRD ARL WM BC
A ZIELINSKI
AMSRD ARL WM BE
S L HOWARD
AMSRD ARL WM BD
A J KOTLAR
AMSRD ARL WM MD
G GAZONAS
C HOPPEL
AMSRD ARL WM MC
E CHIN
J LASALVIA
AMSRD ARL WM T
B BURNS
T W WRIGHT
W GILLICH
AMSRD ARL WM TA
T HAVEL
M BURKINS
N GNIAZDOWSKI
W A GOOCH
E HORWATH
D KLEPONIS
B LEAVY
M NORMANDIA
J RUNYEON
G SILSBY

NO. OF
COPIES ORGANIZATION

ABERDEEN PROVING GROUND (CONT'D)

AMSRD ARL WM TB
P BAKER
R BITTING
R LOTTERO
J STARKENBERG
AMSRD ARL WM TC
R COATES
J BARB
N BRUCHEY
M FERMEN COKER
E KENNEDY
K KIMSEY
L MAGNESS
D SCHEFFLER
S SCHRAML
B SORENSEN
R SUMMERS
W WALTERS
G RANDERS PEHRSON (LLNL)
AMSRD ARL WM TD
S SCHOENFELD
S R BILYK
T W BJERKE
D CASEM
J CLAYTON
D DANDEKAR
M GREENFIELD
Y I HUANG
H KANG
R KRAFT
H W MEYER
M RAFTENBERG
E RAPACKI
M SCHEIDLER
S SEGLETES (3 CPS)
T WEERISOORIYA
AMSRD ARL WM TE
J POWELL
A PRAKASH

<u>NO. OF COPIES</u>	<u>ORGANIZATION</u>	<u>NO. OF COPIES</u>	<u>ORGANIZATION</u>
2	AERONAUTICAL & MARITIME RESEARCH LABORATORY S CIMPOERU D PAUL PO BOX 4331 MELBOURNE VIC 3001 AUSTRALIA	1	CEA R CHERET CEDEX 15 313 33 RUE DE LA FEDERATION PARIS 75752 FRANCE
1	DSTO AMRL WEAPONS SYSTEMS DIVISION N BURMAN (RLLWS) SALISBURY SOUTH AUSTRALIA 5108 AUSTRALIA	1	CEA/CESTA A GEILLE BOX 2 LE BARP 33114 FRANCE
1	ROYAL MILITARY ACADEMY G DYCKMANS RENAISSANCELAAN 30 1000 BRUSSELS BELGIUM	5	CENTRE D ETUDES DE GRAMAT C LOUPIAS P OUTREBON J CAGNOUX C GALLIC J TRANCHET GRAMAT 46500 FRANCE
1	BULGARIAN ACADEMY OF SCI SPACE RESEARCH INSTITUTE V GOSPODINOV 1000 SOFIA PO BOX 799 BULGARIA	6	CENTRE DE RECHERCHES ET D'ETUDES D'ARCUEIL D BOUVART C COTTENNOT S JONNEAUX H ORSINI S SERROR F TARDIVAL 16 BIS AVENUE PRIEUR DE LA COTE D'OR F94114 ARCUEIL CEDEX FRANCE
1	CANADIAN ARSENALS LTD P PELLETIER 5 MONTEE DES ARSENAUX VILLIE DE GRADEUR PQ J5Z2 CANADA	1	DAT ETBS CETAM C ALTMAYER ROUTE DE GUERRY BOURGES 18015 FRANCE
1	DEFENCE RSCH ESTAB SUFFIELD D MACKAY RALSTON ALBERTA TOJ 2NO RALSTON CANADA	1	ETBS DSTI P BARNIER ROUTE DE GUERAY BOITE POSTALE 712 18015 BOURGES CEDEX FRANCE
1	DEFENCE RSCH ESTAB SUFFIELD C WEICKERT BOX 4000 MEDICINE HAT ALBERTA TIA 8K6 CANADA	1	FRENCH GERMAN RESEARCH INST P Y CHANTERET CEDEX 12 RUE DE L'INDUSTRIE BP 301 F68301 SAINT LOUIS FRANCE
1	DEFENCE RSCH ESTAB VALCARTIER ARMAMENTS DIVISION R DELAGRAVE 2459 PIE X1 BLVD N PO BOX 8800 CORCELETTE QUEBEC GOA 1R0 CANADA		

<u>NO. OF COPIES</u>	<u>ORGANIZATION</u>	<u>NO. OF COPIES</u>	<u>ORGANIZATION</u>
5	FRENCH GERMAN RESEARCH INST H J ERNST F JAMET P LEHMANN K HOOG H F LEHR CEDEX 5 5 RUE DU GENERAL CASSAGNOU SAINT LOUIS 68301 FRANCE	2	IABG M BORRMANN H G DORSCH EINSTEINSTRASSE 20 D 8012 OTTOBRUN B MUENCHEN GERMANY
1	CONDAT J KIERMEIR MAXIMILIANSTR 28 8069 SCHEYERN FERNHAG GERMANY	1	INGENIEURBUERO DEISENROTH AUF DE HARDT 33 35 D5204 LOHMAR 1 GERMANY
1	DIEHL GBMH AND CO M SCHILDKNECHT FISCHBACHSTRASSE 16 D 90552 ROETBENBACH AD PEGNITZ GERMANY	1	TU MUENCHEN E IGENBERGS ARCISSTRASSE 21 8000 MUENCHEN 2 GERMANY
4	ERNST MACH INST V HOHLER E SCHMOLINSKE E SCHNEIDER K THOMA ECKERSTRASSE 4 D 7800 FREIBURG I BR 791 4 GERMANY	1	NATIONAL GEOPHYSICAL RESEARCH INSTITUTE G PARTHASARATHY HYDERABAD 500 007 (A P) INDIA
3	FRAUNHOFER INST FUER KURZZEITDYNAMIK ERNST MACH INSTITUT H ROTHENHAEUSLER H SENF E STRASSBURGER KLINGELBERG 1 D79588 EFRINGEN KIRCHEN GERMANY	5	UNIVERSITY OF ROORKEE DEPARTMENT OF PHYSICS N DASS ROORKEE 247 667 INDIA
3	FRENCH GERMAN RESEARCH INST G WEIHRAUCH R HUNKLER E WOLLMANN POSTFACH 1260 WEIL AM RHEIN D 79574 GERMANY	1	RAFAEL BALLISTICS CENTER E DEKEL Y PARTOM G ROSENBERG Z ROSENBERG Y YESHURUN PO BOX 2250 HAIFA 31021 ISRAEL
		1	TECHNION INST OF TECH FACULTY OF MECH ENGN S BODNER TECHNION CITY HAIFA 32000 ISRAEL
		1	IHI RESEARCH INST STRUCTURE & STRENGTH T SHIBUE 1 15 TOYOSU 3 KOTO TOKYO 135 JAPAN

<u>NO. OF COPIES</u>	<u>ORGANIZATION</u>	<u>NO. OF COPIES</u>	<u>ORGANIZATION</u>
1	ESTEC CS D CASWELL BOX 200 NOORDWIJK 2200 AG NETHERLANDS	2	IOFFE PHYSICO TECHNICAL INSTITUTE DENSE PLASMA DYNAMICS LABORATORY E M DROBYSHEVSKI A KOZHUSHKO ST PETERSBURG 194021 RUSSIAN REPUBLIC
4	PRINS MAURITS LABORATORY H J REITSMA E VAN RIET H PASMAN R YSSELSTEIN TNO BOX 45 RIJSWIJK 2280AA NETHERLANDS	1	IPE RAS A A BOGOMAZ DVORTSOVAIA NAB 18 ST PETERSBURG RUSSIAN REPUBLIC
1	ROYAL NETHERLANDS ARMY J HOENEVELD V D BURCHLAAN 31 PO BOX 90822 2509 LS THE HAGUE NETHERLANDS	2	LAVRENTYEV INST HYDRODYNAMICS L A MERZHIEVSKY V V SILVESTROV 630090 NOVOSIBIRSK RUSSIAN REPUBLIC
1	INST OF CHEMICAL PHYSICS A YU DOLGOBORODOV KOSYGIN ST 4 V 334 MOSCOW RUSSIAN REPUBLIC	1	MOSCOW INST OF PHYSICS & TECH S V UTUZHNIKOV DEPT OF COMPUTATIONAL MATHEMATICS DOLGOPRUDNY 1471700 RUSSIAN REPUBLIC
4	INST OF CHEMICAL PHYSICS RUSSIAN ACADEMY OF SCIENCES G I KANEL A M MOLODETS S V RAZORENOV A V UTKIN 142432 CHERNOGOLOVKA MOSCOW REGION RUSSIAN REPUBLIC	1	RESEARCH INSTITUTE OF MECHANICS NIZHNIY NOVGOROD STATE UNIVERSITY A SADYRIN P R GAYARINA 23 KORP 6 NIZHNIY NOVGOROD 603600 RUSSIAN REPUBLIC
3	INST OF MECH ENGINEERING PROBLEMS V BULATOV D INDEITSEV Y MESCHERYAKOV BOLSHOY 61 V O ST PETERSBURG 199178 RUSSIAN REPUBLIC	2	RUSSIAN FEDERAL NUCLEAR CENTER VNIIEF L F GUDARENKO R F TRUNIN MIRA AVE 37 SAROV 607190 RUSSIAN REPUBLIC
1	INST OF MINEROLOGY & PETROGRAPHY V A DREBUSHCHAK UNIVERSITETSKI PROSPEKT 3 630090 NOVOSIBIRSK RUSSIAN REPUBLIC		

<u>NO. OF COPIES</u>	<u>ORGANIZATION</u>	<u>NO. OF COPIES</u>	<u>ORGANIZATION</u>
1	ST PETERSBURG STATE TECHNICAL UNIVERSITY FACULTY OF PHYSICS AND MECHANICS DEP OF THEORETICAL MECHANICS A KRIVTSOV POLITECHNICHESKAYA STREET 29 195251 ST PETERSBURG RUSSIAN REPUBLIC	2	K&W THUN W LANZ W ODERMATT ALLMENDSSTRASSE 86 CH 3602 THUN SWITZERLAND
1	SAMARA STATE AEROSPACE UNIV L G LUKASHEV SAMARA RUSSIAN REPUBLIC	2	AWE M GERMAN W HARRISON FOULNESS ESSEX SS3 9XE UNITED KINGDOM
1	UNIVERSIDAD DE CANTABRIA FACULTAD DE CIENCIAS DEPARTAMENTO DE FISICA APLICADA J AMOROS AVDA DE LOS CASTROS S/N 39005 SANTANDER SPAIN	1	CENTURY DYNAMICS LTD N FRANCIS DYNAMICS HOUSE HURST RD HORSHAM WEST SUSSEX RH12 2DT UNITED KINGDOM
1	DYNAMEC RESEARCH AB A PERSSON PO BOX 201 S 151 23 SODERTALJE SWEDEN	5	DERA I CULLIS J P CURTIS Q13 A HART Q13 K COWAN Q13 M FIRTH R31 FORT HALSTEAD SEVENOAKS KENT TN14 7BP UNITED KINGDOM
7	FOI SWEDISH DEFENCE RESEARCH AGENCY GRINDSJON RESEARCH CENTRE L GUNNAR OLSSON B JANZON G WIJK R HOLMLIN C LAMNEVIK L FAST M JACOB SE 147 25 TUMBA SWEDEN	6	DEFENCE RESEARCH AGENCY W A J CARSON I CROUCH C FREW T HAWKINS B JAMES B SHRUBSALL CHOBHAM LANE CHERTSEY SURREY KT16 0EE UNITED KINGDOM
2	SWEDISH DEFENCE RSCH ESTAB DIVISION OF MATERIALS S J SAVAGE J ERIKSON STOCKHOLM S 17290 SWEDEN	1	UK MINISTRY OF DEFENCE G J CAMBRAY CBDE PORTON DOWN SALISBURY WILTSHIRE SP9 0JQ UNITED KINGDOM

NO. OF
COPIES ORGANIZATION

- 1 K TSEMBELIS
SHOCK PHYSICS GROUP
CAVENDISH LABORATORY
PHYSICS & CHEMISTRY OF SOLIDS
UNIVERSITY OF CAMBRIDGE
CAMBRIDGE CB3 0HE
UNITED KINGDOM
- 2 UNIVERSITY OF KENT
PHYSICS LABORATORY
UNIT FOR SPACE SCIENCES
P GENTA
P RATCLIFF
CANTERBURY KENT CT2 7NR
UNITED KINGDOM
- 7 INST FOR PROBLEMS IN
MATERIALS SCIENCE
S FIRSTOV
B GALANOV
O GRIGORIEV
V KARTUZOV
V KOVTUN
Y MILMAN
V TREFILOV
3 KRHYZHANOVSKY STR
252142 KIEV 142
UKRAINE
- 1 INST FOR PROBLEMS OF
STRENGTH
G STEPANOV
TIMIRYAZEVSKEY STR 2
252014 KIEV
UKRAINE

INTENTIONALLY LEFT BLANK.